Journal Pre-proofs

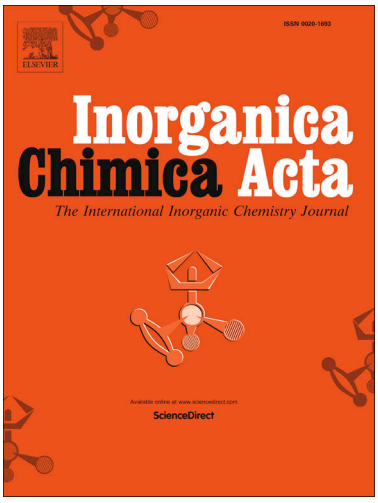

Research paper

A novel *O*-phenanthroline-based bis(half-salamo)-like chemical sensor: For rapid and efficient continuous recognition of Cu^{2+}, HPO_4^{2-} and $H_2PO_4^-$

Ruo-Nan Bian, Xin Xu, Tao Feng, Wen-Kui Dong

PII: S0020-1693(20)31298-6
DOI: https://doi.org/10.1016/j.ica.2020.120098
Reference: ICA 120098

To appear in: *Inorganica Chimica Acta*

Received Date: 3 August 2020
Revised Date: 12 October 2020
Accepted Date: 20 October 2020

Please cite this article as: R-N. Bian, X. Xu, T. Feng, W-K. Dong, A novel *O*-phenanthroline-based bis(half-salamo)-like chemical sensor: For rapid and efficient continuous recognition of Cu^{2+}, HPO_4^{2-} and $H_2PO_4^-$, *Inorganica Chimica Acta* (2020), doi: https://doi.org/10.1016/j.ica.2020.120098

A novel *O*-phenanthroline-based bis(half-salamo)-like chemical sensor: For rapid and efficient continuous recognition of Cu^{2+}, HPO_4^{2-} and $H_2PO_4^-$

Ruo-Nan Bian, Xin Xu, Tao Feng, Wen-Kui Dong*

School of Chemical and Biological Engineering, Lanzhou Jiaotong University, Lanzhou, Gansu 730070, China

A B S T R A C T

A novel *O*-phenanthroline-based bis(half-salamo)-like fluorescent chemical sensor **LPOV** with two N_3O coordination sites was synthesized. These N_3O coordination sites were used for binding to specific metal ions. The sensor **Lpov** can detect Cu^{2+} by the phenomenon of fluorescence quenching and the **Lpov-3Cu^{2+}** complex can detect HPO_4^{2-} and $H_2PO_4^-$ within the detection range. By combining and calculating the experimental results, the recognition mechanism of the sensor for the corresponding ion detection is proposed and the DFT calculation is carried out. The LOD = 7.22×10^{-6} M, LOQ = 2.41×10^{-5} M and the binding constant Ka (Ka = 2.29×10^{13} M^{-1}) of **Lpov** were calculated. The order of the binding constant is as high as 10^{13}, which indicates that the **Lpov-3Cu^{2+}** complex generated by the reaction of the fluorescent chemical sensor **Lpov** with Cu^{2+} is extremely stable.

Keywords: *O*-phenanthroline; bis(half-salamo)-like sensor; hydrogen phosphate; DFT calculation; water quality monitoring[1]

1. Introduction

* Corresponding author. Fax: +86 931 4938703.
E-mail addresses: dongwk@126.com (W.-K. Dong).

The world is enriched by ions, but excess ions can also be a burden on the environment and human life. For example, the addition of copper (II) ions to swimming pools can have a sterilizing effect and copper is a component of many important enzymes in the body that can promote the absorption and utilization of iron can maintain the function of the central nervous system. However, when excess copper remains in the body, it tends to put a strain on the body's organs, especially the liver and gall bladder [1-8]. When there are problems with these two organs, maintaining the body's metabolism can lead to disorders, cirrhosis, ascites or even worse [9-13]. Phosphates are important in inorganic chemistry, biochemistry, and biogeochemistry, but in excess, they can trigger red tide. They contaminate the soil and further affect the crops, putting human health at risk [14-16]. Fluorescent chemical sensors have become popular in recent years in the field of ion detection because they can be used to measure ion rapidly and accurately through changes in fluorescence intensity. The convenient detection of the corresponding ions has attracted increased attention [17-23]. *O*-phenanthroline combines with metal ions to form chelates easily, and the products are more stable [24-29].

Since *O*-phenanthroline and its derivatives can be used as a kind of common excellent fluorescent chemical sensors for subsequent fluorescence detection work, here, we have introduced *O*-phenanthroline into the design of half-salamo-like probe molecules. It is the first time to synthesize half-salamo-like probe molecules with *O*-phenanthroline, unprecedented. Two N and one O atoms from one half-salamo-like unit and one N atom on *O*-phenanthroline can form together one N_3O coordination sites, and used as binding sites for identifying specific metal ions. Half-salamo-based compounds provide a more stable and flexible sensor structure due to the introduction of oxygen atoms that are more electronegative compared to half-salen-based compounds [30-35]. By introducing different groups, the solubility of the ligands in water system can be adjusted, achieve the purpose of detecting metal ions in environmental water samples.

2. Experimental

2.1. Materials and measurements

Please refer to the *Supporting information* for all experimental instruments and raw materials.

*2.2 Synthesis method of **Lpov***

The synthetic route to **Lpov** is shown in **Scheme 1**.

Scheme 1 Synthesis route to **Lpov**

2.2.1 Synthesis of 1,10-phenanthroline-2,9-dicarbaldehyde

1,10-Phenanthroline-2,9-dicarboxaldehyde was synthesized according to a previously reported method [36-40]. To a double-mouthed round bottom flask, 30 mL of a dioxane solution dissolved in selenium dioxide (4.5 g, 40.55 mmol) was added and placed in a water bath. With a constant-pressure drop funnel, 100 mL of dioxane solution dissolved in neo-copper reagent (3 g, 14.40 mmol) was added drop by drop to the double-bottomed flask. After 12h in the water bath reaction, while hot filter out the tar and selenium collection filtrate, the filtrate was yellow. When the filtrate was cooled, a large number of yellow precipitates were generated, namely 1,10-phenanthroline-2,9-dicarboxaldehyde crude product. After filtering out the crude product, it was collected and dissolved in benzene, to which n-hexane was added for recrystallization. Finally, the resulting product was filtered and dried to obtain a golden yellow needle-like solid. Golden yellow needle-like solid 3.1313 g, yield: 81.75%. M.p.: 238-240 °C. Anal. Calcd. for $C_{14}H_8N_2O_2$ (%): C, 71.18; H, 3.41; N, 11.86. Found: C, 71.29; H, 3.25; N, 11.62. ^{1}H NMR (500 MHz, DMSO) δ 10.36 (d, J = 0.8 Hz, 1H), 8.80 (dd, J = 8.2, 0.8 Hz, 1H), 8.32 (d, J = 8.2 Hz, 1H), 8.29 (s, 1H).

2.2.2 Synthesis of 2-[O-(1-Ethyloxyamide)]oxime-6-methoxyphenol

2-[*O*-(1-Ethyloxyamide)]oxime-6-methoxyphenol was prepared according to a

previously reported method [41-46]. Weighing 1,2-bis(aminooxy)ethane 414.45 mg (4.5 mmol) in ethanol (20 mL), another 684.67 mg (4.5 mmol) of 3-methoxysalicylaldehyde was dissolved in ethanol (20 mL). An ethanol solution of 3-methoxysalicylaldehyde was added drop by drop to an ethanol solution of 1,2-bis(aminooxy)ethane in a water bath at 55°C, with a controlled drop acceleration of about 10 s a drop and continuous reaction for 6 h to obtain light yellow ethanol solution. Decompression distillation removes excess solvent and concentrates the reaction solution to about 5 mL. The concentrated solution is a bright yellow oily liquid, further purified by column chromatography to obtain white solid 748.44 mg, yield: 73.51%; M.p.: 95.5-96.5°C. Anal. Calcd. for $C_{10}H_{14}N_2O_4$ (%): C, 53.09; H, 6.24; N, 12.38. Found: C, 53.32; H, 6.20; N, 12.16. ^{1}H NMR (500 MHz, $CDCl_3$) δ 3.92 (s, 3H), 3.96 (t, J = 4.5 Hz, 2H), 4.38 (t, J = 4.5 Hz, 2H), 5.50 (brs, 2H), 6.82 (dd, J = 7.8, 1.6 Hz, 1H), 6.87 (t, J = 7.8 Hz, 1H), 6.90 (dd, J = 7.8, 1.6 Hz, 1H), 8.24 (s, 1H), 9.88 (s, 1H).

*2.2.3 Synthesis of **Lpov***

Lpov was synthesized using the one-pot method. 2-[*O*-(1-Ethyloxyamide)]oxime-6-methoxyphenol (453 mg, 2.0 mmol) and 1,10-phenanthroline-2,9-dicarboxaldehyde (236 mg, 1.0 mmol) were dissolved in the ethanol (20 mL), respectively. The reaction was stirred at 55℃ for 6 h. At the end of the reaction, a large amount of yellowish precipitate is generated at the bottom of the round bottom flask. The product is filter-dried. Light yellow solid: 517.23 mg. M.p.: 145-148°C. Yield: 79.25%. Anal. calcd. for $C_{34}H_{32}N_6O_8$ (%): C, 62.57; H, 4.94; N, 12.88. Found: C, 62.82; H, 4.75; N, 12.67. ^{1}H NMR (500 MHz, DMSO) δ 9.41 (s , 2H), 8.52 (dd, J = 18.5, 15.5 Hz, 6H), 8.19 (d, J = 8.4 Hz, 2H), 8.06 (s, 2H), 7.17 (d, J = 7.9 Hz, 2H), 7.00 (d, J = 9.1 Hz, 2H), 6.81 (t, J = 8.0 Hz, 2H), 4.55 (dd , J = 5.7, 2.9 Hz, 4H), 4.48 (dd, J = 5.6, 3.0 Hz, 4H), 3.80 (s, 6H).

2.3 Experimental methods

2.3.1 Preparation of the required solutions

The metal cations used in this experiment are all nitrates and the anions are all sodium salts. Altogether 16 cations and 16 anions were used, respectively Li^+, Na^+, Ag^+, K^+, Cr^{3+}, Fe^{3+}, Ca^{2+}, Zn^{2+}, Mg^{2+}, Sr^{2+}, Ba^{2+}, Cu^{2+}, Ni^{2+}, Cd^{2+}, Co^{2+} and Al^{3+}, respectively. The anions are Cl^-, $H_2PO_4^-$, I^-, F^-, CN^-, CH_3COO^-, HS^-, NO_3^-, S^{2-}, HCO_3^-, Br^-, $P_2O_7^{4-}$, CO_3^{2-}, ClO_4^-, $B_4O_7^{2-}$ and HPO_4^{2-}.

All salts were configured with distilled water at a concentration of 1×10^{-2} mol/L. **Lpov** was used with V_{DMF}:V_{Water} = 9:1 solution was configured at a concentration of 1×10^{-3} mol/L. The pH of the buffer solution was adjusted using a pHS-45 model acidimeter.

2.3.2 Fluorescence spectroscopy experiments

Fresh Tris-HCl buffer solution was used for all the measurements of fluorescence spectra. The ions were added in an amount 20 times greater than **Lpov** and diluted with the buffer solution so that **Lpov** in the cuvette was mixed with the ions. The concentration of the solution was 1×10^{-5} mol/L.

2.3.3 Determination of Job Work Curves

Keeping the total concentrations of **Lpov** and constant while measuring the Job work curve, will The concentrations of **Lpov** and $Cu(NO_3)\cdot3H_2O$ were adjusted in the following ratios 1:9, 2:8, 3:7, 4:6, 5:5, 6:4, 7:3, 8:2, 9:1, and 10:0. Configure the desired solution according to the ratios and stir at room temperature for 4h. The configured solutions under the same conditions were measured, the fluorescence data at 382 nm were recorded, and the Job work curves were plotted according to the data obtained.

2.3.4 ESI-MS spectrum sample

Lpov (0.05 mmol, 32.64 mg) and $Cu(NO_3)_2$ (0.25 mmol, 46.89 mg) were dissolved in trichloromethane solution, stirred for 6h. Evaporated and concentrated to obtain solid powder, it's the complex **Lpov-3Cu^{2+}**. **Lpov-3Cu^{2+}** (0.03 mmol, 25.24 mg) and NaH_2PO_4 (0.15 mmol, 17.98 mg) / Na_2HPO_4 (0.15 mmol, 21.29 mg) were

dissolved in trichloromethane solution, stirred for 6h. Evaporated and concentrated to obtain solid powder, it's the complex **[Lpov-Cu^{2+}]-$H_2PO_4^-$** / **[Lpov-Cu^{2+}]-HPO_4^{2-}**.

3. Results and discussion

*3.1 Solubility testing and characterization of **Lpov***

The solubilities of the sensor in common organic solvents were tested. **Lpov** was dissolved in dichloromethane, trichloromethane, DMSO (dimethyl sulfoxide), EA (ethyl acetate), py (pyridine), THF (tetrahydrofuran) and DMF (N,N-dimethylformamide) at room temperature. Three methods were used to characterize **Lpov**: ^{1}H NMR, ^{13}C NMR and ESI-MS. Through the comprehensive analysis of the spectrum results (*Supporting information*), it is determined that the synthesized powder solid is the target product **Lpov**.

*3.2 Fluorescent chemical behavior of **Lpov** and the effect of metal ions*

Solvent effect is an important factor affecting the photochemical behavior of fluorescent chemical sensors [47-51]. First, a solution of the same concentration of **Lpov** dissolved in different organic solvents was prepared to compare the fluorescence in different organic solvents behavior. The experimental results are shown in **Fig. 1**, from which it can be seen that the **Lpov** emits the highest fluorescence intensity in DMF, thus DMF was chosen as a solvent for later probing the chemical behavior of **Lpov** fluorescence.

Fig. 1 Effect of the solvent system on the fluorescence intensity of the **Lpov**

A set of experiments were made to investigate the effect of water content on the fluorescence of **Lpov**, in order to detect metal ions in ambient water samples. Formulated at DMF:H_2O ratios of 9:1, 8:2, 7:3, 6:4, 5:5, 4:6 solvent, weighing the same mass of **Lpov** and dissolving it in prepared DMF:H_2O solutions of different ratios, it was found that **Lpov** is not completely soluble in a solution with a ratio of

4:6, so the fluorescence measurement of that ratio was abandoned. To test the fluorescence intensity of the same concentration **Lpov** solution dissolved in another five proportions, the choice was determined by comparing the peak value DMF: H_2O. The ratio of 9:1 was used as the solvent for the subsequent fluorescence spectrum experiment. The experimental results are shown in **Fig. 2**.

Fig. 2 The effect of water content in solvent (DMF:H_2O, v/v) on the fluorescence intensity of **Lpov**

Next, the effect of metal ions on the fluorescence behavior of **Lpov** was investigated in Tris-HCl buffer solution (DMF/H_2O = 9/1, v/v, pH = 7.23), the metal cation full scan fluorescent experiment was carried out (**Fig. 3**). From the analyses of the experimental results, it can be seen that **Lpov** is most severely affected by Cu^{2+}, and the fluorescence intensity quenched the 89.38%. Subsequently, Cu^{2+} titration experiments were completed in order to determine the optimal coordination ratio of **Lpov** to Cu^{2+}. After calculation and analysis of the results, the optimal coordination ratio of **Lpov** to Cu^{2+} was determined to be 1:3. The mass spectral analysis of the **Lpov-3Cu^{2+}** complex (*Supporting information*) also allowed the determination of the coordination ratio of **Lpov** to the optimal coordination ratio of Cu^{2+} is 1:3.

Fig. 3 Fluorescence spectra of **Lpov** and metal ions (20 equiv.) in DMF/H_2O buffer solution (**Lpov**, 1×10^{-3} mol/L; Tris-HCl buffer solution, 9/1, v/v, pH = 7.23)

*3.3 Performance investigation of Cu^{2+} detection by **Lpov***

It can be seen from **Fig. 3** that the fluorescence emission of **Lpov** was the strongest at 382 nm. However, the addition of Cu^{2+} made the maximum emission peak of **Lpov** disappear. In the titration experiment, it was found that with the addition of Cu^{2+}, the titration reached the end point until 3 eq. (**Fig. 4**). Meanwhile, the solution in the cuvette changed from colorless to a dark green visible to the naked eye. Thus, it was evident that **Lpov** has a very excellent ability to recognize Cu^{2+}, and in order to

further develop the performance of **Lpov** to detect Cu^{2+}, the numerical values that LOD (Limit of Detection) and LOQ (Limit of Quantitation) of **Lpov** for Cu^{2+} were calculated based on the processing of titration spectrogram data and previous literature [52-54].

$$\mathrm{LOD} = K \times \delta / S \; ; \; \mathrm{LOQ} = 10 \times \delta / S \; ; \quad \delta = \sqrt{\frac{\sum (F_0 - \overline{F_0})^2}{N-1}} \quad (N = 20);\ K = 3.$$

N in the formula is measured number of times for **Lpov** blank solution and S represents the slope of the fluorescence intensity versus sample concentration curve, K is coefficient determined at a certain level of confidence (IUPAC recommends K = 3 for spectrochemical analysis), where F_0 is the fluorescence intensity of the **Lpov** blank solution (The blank solution is the **Lpov** solution without adding metal ions, c = 1×10^{-3} mol/L). The LOD = 7.22×10^{-6} M and LOQ = 2.41×10^{-5} M of **Lpov** were calculated. Through the titration experiment data, referring to the previous literature and combining the Benesi-Hildebrand equation (1), the value of the binding constant Ka (Ka = 2.29×10^{13} M^{-1}) was calculated [55,56]. The order of the binding constant is as high as 10^{13}, which indicates that the **Lpov-3Cu^{2+}** complex generated by the reaction of **Lpov** with Cu^{2+} is extremely stable.

$$1/(F - F_0) = 1/(F_{max} - F_0)\{(K_a [M^{m+}]^n) + 1\} \qquad (1)$$

F is the fluorescence intensity of the **Lpov-3Cu^{2+}** complex at 382 nm, F_0 is the fluorescence intensity at 382 nm when the Cu^{2+} ion concentration is zero, and F_{max} is the maximum fluorescence intensity at 382 nm (EX WL: 325 nm). $[M^{m+}]$ is the concentration of Cu^{2+} ions and n is the coordination ratio of **Lpov** to Cu^{2+} (n = 3). The Benesi-Hildebrand fit curve of **Lpov** to Cu^{2+} is shown in **Fig. 5** shown.

Fig. 4 Fluorescence titration of Cu^{2+} in DMF/H_2O buffer solution with **Lpov**. (The inset shows a scatter plot of the fluorescence intensity of **Lpov** at 382 nm with Cu^{2+} concentration; **Lpov**, 1×10^{-3} mol/L; Tris-HCl buffer solution, 9/1, v/v, pH = 7.23).

Fig. 5 Benesi-Hildebrand fit curve of Cu^{2+} with **Lpov**

One of the most important indicators for distinguishing the quality of fluorescent chemical sensors is the ability to recognize specific ions without interference from other ions. Therefore, it is very necessary to do anti-interference experiments. Under the same conditions, the anti-interference experiment of **Lpov** to identify Cu^{2+} was conducted. According to the anti-interference experimental data, it can be clearly observed that other metal ions do not interfere with the detection of Cu^{2+}. As shown in **Fig. 6**, the interference of other metal ions on the recognition of Cu^{2+} by **Lpov** can be seen directly from the histogram.

Fig. 6 Lpov (1×10^{-3} mol/L) in DMF/H_2O buffer solution for Cu^{2+} recognition anti-interference experiment. (Emission peak at 382 nm. The black bar is the fluorescence intensity of **Lpov** at 382 nm after adding common metal ion, the red bar is the fluorescence intensity of the **Lpov-3Cu^{2+}** complex after adding common metal ion. **Lpov**, 1×10^{-3} mol/L; cation, 1×10^{-2} mol/L; Tris-HCl buffer solution, 9/1, v/v, pH = 7.23).

The wider pH range of the sensor, the wider the range of applications. As shown in **Fig. 7**, the pH application range of **Lpov** was studied. The change of fluorescence intensity of **Lpov** and Cu^{2+} was tested under the condition of pH = 2 ~ 13. According to the experimental data, the change of fluorescence intensity of **Lpov** and Cu^{2+} was relatively stable in the range of pH = 4 ~ 8, which indicated that the recognition effect of **Lpov** on Cu^{2+} was very stable in a wide range of pH.

Fluorescent chemical sensors have the advantage of fast response times, eliminating tedious testing times and allowing chemical sensors to dominate in various applications. The response time of **Lpov** to Cu^{2+} was tested. After the change of fluorescence intensity and time statistics, it was found that the response time of **Lpov** to Cu^{2+} was very short. The response time is approximately 10 s, and the fluorescence tends to stabilize after 10 s, as shown in **Fig. 8**.

Fig. 7 The pH response of **Lpov** and Cu^{2+} in fluorescent chemical sensors (**Lpov**, 1×10^{-3} mol/L; Tris-HCl buffer solution, 9/1, v/v)

Fig. 8 Time response diagram of interaction between **Lpov** and Cu^{2+} in fluorescent chemical sensor (**Lpov**, 1×10^{-3} mol/L; Tris-HCl buffer solution, 9/1, v/v, pH = 7.23).

To further verify the optimal coordination ratio of **Lpov** to Cu^{2+}, Job working curves were measured and plotted. As shown in **Fig. 9**, at the excitation wavelength of 325 nm, the fluorescence intensity of **Lpov** exhibits a turning point at the mass fraction (Cu^{2+}) of 0.75. The results indicated that the optimal coordination ratio of **Lpov** to Cu^{2+} should be 1:3. The mass spectrogram of the **Lpov-3Cu^{2+}** complex can also be used to infer the optimal coordination ratio of **Lpov** to Cu^{2+}, as shown in **Fig. 10**. As can be seen in the mass spectra, m/z = 838.1234 is the molecular ion peak of **[Lpov+3Cu^{2+}]$^{4+}$**. Compared with other references [57,58], it is found that the binding constant of **Lpov** for Cu^{2+} recognition is larger, which indicates that the copper(II) complex of **Lpov** is more stable. In addition, the LOD of the chemical sensor **Lpov** is smaller than those of other Cu^{2+} probes in the literatures, indicating that the chemical sensor is more sensitive to recognize Cu^{2+}. Binding constants and detection lines between the related chemosensors mentioned in literatures are compared, as shown in **Table 1**.

Fig. 9 Job working curve of Cu^{2+} on **Lpov** (**Lpov**, 1×10^{-3} mol/L; Tris-HCl buffer solution, 9/1, v/v, pH = 7.23)

Fig. 10 ESI-MS spectrum (a) ESI-MS spectrum of **Lpov**; (b) ESI-MS spectrum of the **Lpov-3Cu^{2+}** complex

Table 1 Comparison of binding constants and detection lines between the chemosensors.

*3.4 Mechanism of recognition of Cu^{2+} by **Lpov***

The stability order of complexes generated from divalent Mn^{2+} to Zn^{2+} with ligands containing N coordination atoms can be observed in the following order: $Mn^{2+}<Fe^{2+}<Co^{2+}<Ni^{2+}<Zn^{2+}<Cu^{2+}$, the sequence called the Irving-Williams sequence, which roughly corresponds to the variation of the weak-field CFSE [59,60]. According to Jahn-Teller effect, there are three electrons in the two degenerate d orbitals (Eg) of divalent copper (II) ions in octahedral complexes due to the splitting of crystal field. The number of electrons occupied in these two orbitals is different, and the complex is a nonlinear molecule, which leads to the splitting of Eg [61]. The results of splitting lead to Jahn-Teller distortion, and the Irving-Williams (CFSE increase) order obtained from the crystal field splitting energy is abnormal, which leads to the **Lpov-3Cu^{2+}** complex being more stable than other divalent metal (II) complexes in the same period.

The effect of the complexes in different oxidation states on the charge density is linear, indicating that there is a strong relationship between the charge density around the metal and the oxidation state [62,63]. In the presence of Cu^{2+}, the fluorescence intensity of the system is quenched. This indicates that Cu^{2+} interacts with the system effectively and has the photoinduced electron transfer (PET) effect, which reduces the fluorescence intensity.

Based on the Irving-Williams sequence, the copper (II) complexes are more stable in comparison to those of other same period divalent metal ions. Based on all the above experimental results, a mechanism for **Lpov** to recognize Cu^{2+} was proposed. Compared with oxygen atoms, the electronegativity of N atoms is relatively small, the ability to attract electrons is relatively weak, and it is easy to give electrons, so the coordination ability of N atoms is stronger than that of O atoms [64,65]. When **Lpov** was combined with three Cu^{2+} ions, the two Cu^{2+} ions are respectively combined with the N_3O coordination sites, which makes **Lpov** present a spiral structure. After the sensor molecular screwed, a larger coordination site was formed in the middle, and the last Cu^{2+} entered the coordination site to combine with four N

atoms, and finally formed a 1:3 type complex. Mechanism of recognition of Cu^{2+} by **Lpov** is shown in **Fig. 11**.

Fig. 11 Proposed recognition mechanism of Cu^{2+} by **Lpov**

*3.5 Computational procedure for **Lpov-3Cu^{2+}** complex*

For the structures of the ligand and its complexes, full optimization was performed by Density Functional Theory (DFT) using Gaussian'09.

The calculation results of **LPOV** showed that the molecular orbital No.171 is a HOMO orbital, E_{171} = -5.85798 eV, the molecular orbital No.172 is a LUMO orbital, E_{172} = -2.16327 eV, and the energy gap ΔE = E_{172} - E_{171} = 3.69471 eV, the energy gap is large. In order to fully analyze the charge density distribution, choose to calculate the electron cloud and distribution of LUMO+2 (174), LUMO+1 (173), LUMO (172), HOMO (171), HOMO-1 (170), HOMO-2 (169) orbits respectively (**Fig. 12a**). It can be seen from the figure that the HOMO, LUMO of **LPOV** and the electron clouds in the adjacent orbits are mostly distributed locally. LUMO and LUMO+1 orbital electron clouds were mainly distributed on the part of *O*-phenanthroline. HOMO and HOMO-1 orbital electron clouds were mainly distributed on the half-salamo-like part. HOMO-2 and LUMO+2 orbital electron clouds were mainly distributed on the half-salamo-like part and the part of *O*-phenanthroline.

For the α-spin orbit of the **Lpov-3Cu^{2+}** complex, the molecular orbital No.199 is the HOMO orbital, E_{199} = -3.05712 eV, the molecular orbital No.200 is the LUMO orbital, E_{200} = -1.83946 eV and the energy gap ΔE = E_{200} - E_{199} = 1.21766 eV. In order to fully analyze the charge density distribution, select the LUMO+2 (202), LUMO+1 (201), LUMO (200), HOMO (199), HOMO-1 (198), HOMO-2 (197) orbits to calculate the electron cloud and distribution (**Fig. 12b**). It can be seen from the figure that the HOMO, LUMO of the α-spin orbit of the **Lpov-3Cu^{2+}** complex and the electron clouds in the adjacent orbit mostly show local distribution. HOMO and LUMO orbital electron clouds were mainly distributed on the benzene ring part of the *O*-phenanthroline. For the β-spin orbital of the **Lpov-3Cu^{2+}** complex, the molecular

orbital No.198 is the HOMO orbital, E_{198} = -3.77036 eV, the molecular orbital No.199 is the LUMO orbital, E_{199} = -1.83484 eV, and the energy gap ΔE = E_{199} - E_{198} = 1.93552 eV. In order to fully analyze the charge density distribution, choose to calculate the electron cloud and distribution of LUMO+2 (201), LUMO+1 (200), LUMO (199), HOMO (198), HOMO-1 (197), HOMO-2 (196) orbits respectively (**Fig. 12b**). It can be seen from the figure that the HOMO, LUMO of the β-spin orbit of the **Lpov-3Cu^{2+}** complex and the electron clouds in the adjacent orbit mostly show local distribution. The HOMO electron cloud was mainly distributed on the the terminal group of the *O*-phenanthroline and Cu (II) atom. The LUMO electron cloud is mainly distributed on the part of *O*-phenanthroline.

Fig. 12 Molecular orbital energy diagrams of **L$_{POV}$** and the **Lpov-3Cu^{2+}** complex. (a) Molecular orbital energy diagram of **L$_{POV}$**. (b) Molecular orbital energy diagram of the **Lpov-3Cu^{2+}** complex

3.6 Detection of Cu^{2+} in tap water samples

Copper (II) ions in drinking water are often caused by water leaching from copper (II) pipes, and high levels of dissolved oxygen can accelerate copper corrosion. The tap water sample experiment was used to verify the practicability of **Lpov**. A known amount of Cu^{2+} was added to the tap water as the tap water sample. After adding **Lpov**, the recovery rate was calculated based on the measured fluorescence intensity, as shown in **Fig. 13**. The recovery rate ranges from 98.3% to 101.25% and the relative standard deviation is controlled within 3%. The results of this experiment proved that **Lpov** can be used for the determination of Cu^{2+} in tap water.

Fig. 13 Determination of Cu^{2+} in tap water sample (n = 3; **Lpov**, 1×10^{-3} mol/L).

*3.7 Study on the performance of detecting HPO_4^{2-} and $H_2PO_4^-$ with the **Lpov-3Cu^{2+}** complex*

After experimental research on Cu^{2+} detection, the **Lpov-3Cu^{2+}** complex was unexpectedly found to have good selectivity for $HPO_4^{2-}/H_2PO_4^-$ in the anion anti-interference experiment. The anions of HPO_4^{2-} and $H_2PO_4^-$ are important buffer pairs in the living system, which can maintain a certain pH value, thus ensuring the stability of the blood of the living body. First, the anion anti-interference experiment of **Lpov** to Cu^{2+} was done in Tris-HCl buffer solution, as shown in **Fig. 14**. After adding HPO_4^{2-} to the **Lpov-3Cu^{2+}** complex, the fluorescence intensity increased by 970.83%, and after adding $H_2PO_4^-$, the fluorescence intensity increased by 427.08%. However, the fluorescence intensity after adding other anions was not much different from that of the **Lpov-3Cu^{2+}** complex. Therefore, using the **Lpov-3Cu^{2+}** complex as a new sensor, it can continue to recognize $HPO_4^{2-}/H_2PO_4^-$ with remarkable recognition.

*3.8 Titration of the **Lpov-3Cu^{2+}** complex to **2Lpov-Cu^{2+}** and Job work curves*

To determine the coordination ratio of the ***Lpov-3Cu^{2+}*** complex to $HPO_4^{2-}/H_2PO_4^-$, take HPO_4^{2-} as an example, the ***Lpov-3Cu^{2+}*** complex was titrated against HPO_4^{2-} (as shown in **Fig. S6**). The processing of the titration experimental data and the summary of the mass spectrometry data revealed that the **Lpov-3Cu^{2+}** complex with HPO_4^{2-} both with an optimal coordination ratio of 1:1. At the same time, the results of the Job working curve experiment also proved that the optimal coordination ratio of **[Lpov+3Cu^{2+}]$^{4+}$** to HPO_4^{2-} is 1:1 (as shown in **Fig. S7**), which laid a foundation for the later mechanism exploration. Reference to other literatures [66,67], comparison of binding constants and detection lines between the chemosensors is shown in **Table 1**.

Fig. 14 The **Lpov-3Cu^{2+}** complex (1×10^{-3} mol/L) in DMF/H_2O buffer solution for $HPO_4^{2-}/H_2PO_4^-$ recognition anti-interference experiment. (Emission peak at 382 nm. The black bar is the fluorescence intensity of **L$_{POV}$**, the red bar is the fluorescence intensity of **L$_{POV}$** with Cu^{2+} added, the blue bar is the fluorescence intensity of the **Lpov-3Cu^{2+}** complex after adding common metal anions, the pink bar is the

fluorescence intensity of **LPOV** after adding common metal anions. **LPOV**, 1×10^{-3} mol/L; cation, 1×10^{-2} mol/L; Tris-HCl buffer solution, 9/1, v/v, pH = 7.23).

*3.9 Computational procedure for **2Lpov-Cu^{2+}** complex*

For the α-spin orbit of the **2Lpov-Cu^{2+}** complex, the molecular orbital No.351 is the HOMO orbital, E_{351} = -9.25337 eV, the molecular orbital No.352 is the LUMO orbital, E_{352} = -6.62316 eV and the energy gap ΔE = E_{352} - E_{351} = 2.63021 eV. In order to fully analyze the charge density distribution, select the LUMO+2(354), LUMO+1 (353), LUMO (352), HOMO (351), HOMO-1 (350), HOMO-2 (349) orbits to calculate the electron cloud and distribution (**Fig. 15**). It can be seen from the figure that the HOMO, LUMO of the α-spin orbit of the **2Lpov-Cu^{2+}** complex and the electron clouds in the adjacent orbit mostly show local distribution. The LUMO orbital electron clouds were mainly distributed on the part of the *O*-phenanthroline. The HOMO orbital electron clouds were mainly distributed on the half-salamo-like part. For the β-spin orbital of the **2Lpov-Cu^{2+}** complex, the molecular orbital No.350 is the HOMO orbital, E_{350} = -8.96004 eV, the molecular orbital No.351 is the LUMO orbital, E_{351} = -8.72330 eV, and the energy gap ΔE = E_{351} - E_{350} = 0.23674 eV. In order to fully analyze the charge density distribution, choose to calculate the electron cloud and distribution of LUMO+2 (353), LUMO+1 (352), LUMO (351), HOMO (350), HOMO-1 (349), HOMO-2 (348) orbits respectively (**Fig. 15**). It can be seen from the figure that the HOMO, LUMO of the β-spin orbit of the **Lpov-3Cu^{2+}** complex and the electron clouds in the adjacent orbit mostly show local distribution. The HOMO and LUMO orbital electron clouds were mainly distributed on the part of the *O*-phenanthroline and Cu(II) atom.

Fig. 15 Molecular orbital energy diagrams of the **2Lpov-Cu^{2+}** complex.

*3.10 On the recognition mechanism of HPO_4^{2-}/$H_2PO_4^-$ by sensor **[Lpov+3Cu^{2+}]$^{4+}$***

It can be inferred from the titration experiments (**Fig. 16**) and Job working curves (**Fig. 17**) that the optimal coordination ratio of **Lpov-3Cu^{2+}** and $H_2PO_4^-$ is 1:1.

The LOD and LOQ of $H_2PO_4^-$ were calculated as per IUPAC guidelines and it was found to be 5.83 ×10^{-8} and 1.96 ×10^{-7} M, respectively. $H_2PO_4^-$ releases two molecules of H^+ through two-step ionization. H^+ combines with the complex **Lpov-3Cu^{2+}**, and then releases Cu^{2+}. The results are consistent with the ESI-MS spectra of complex **[Lpov+3Cu^{2+}]$^{4+}$+H$_2$PO$_4^-$** (**Fig. 18**). This may be due to the relatively small *Ksp* of the product that is generated from PO_4^{3-} with Cu^{2+} [68]. Mechanism of recognition of HPO_4^{2-}/$H_2PO_4^-$ by the **Lpov-3Cu^{2+}** complex is shown in **Fig. 19**.

Fig. 16 Fluorescence titration of $H_2PO_4^-$ in DMF/H_2O buffer solution with the **Lpov-3Cu^{2+}** complex. (The **Lpov-3Cu^{2+}** complex, 1×10^{-3} mol/L; cation, 1×10^{-2} mol/L; Tris-HCl buffer solution, 9/1, v/v, pH = 7.23).

Fig. 17 Job working curve of $H_2PO_4^-$ on the **Lpov-3Cu^{2+}** complex

Fig. 18 ESI-MS spectrum (a) ESI-MS spectrum of the **2Lpov-Cu^{2+}** complex (HPO_4^{2-}); (b) ESI-MS spectrum of the **2Lpov-Cu^{2+}** complex ($H_2PO_4^-$)

Fig. 19 Proposed recognition mechanism of HPO_4^{2-}/$H_2PO_4^-$ by the **Lpov-3Cu^{2+}** complex

4. Conclusions

An *O*-phenanthroline-based bis(half-salamo)-like chemical sensor **Lpov** was synthesized with 2,9-dimethyl-1,10-phenanthroline and 2-[*O*-(1-ethyloxyamide)]oxime-6-methoxyphenol. **Lpov** can detect Cu^{2+} by the phenomenon of fluorescence quenching and the **Lpov-3Cu^{2+}** complex can detect HPO_4^{2-} and $H_2PO_4^-$ within the detection range. Half-salamo-like structure was introduced into *O*-phenanthroline, which makes **Lpov** have two N_3O coordination sites. Different from the traditional N_2O_2 coordination sites of salamo-like compounds, the introduction of N atom of *O*-phenanthroline with stronger coordination ability makes the coordination

mode more novel and provides more possibilities for the coordination modes. By calculation, LOD = 7.2215×10^{-6} M and binding constant Ka = 2.29×10^{13} M^{-1}. The proposed recognition mechanism of the sensor is verified by the results of mass spectrometry and DFT calculations.

Declarations of interest:

The authors declare no conflict of interest.

Acknowledgements

This work was supported by the National Natural Science Foundation of China (21761018) and the Program for Excellent Team of Scientific Research in Lanzhou Jiaotong University (201706), both of which are gratefully acknowledged.

References

[1] P.G. Sutariya, H. Soni, S.A. Gandhi, A. Pandya, New J. Chem. 43 (2019) 9855.

[2] S. Slassi, M. Aarjane, A.E. Ghayoury, A. Amine, Spectrochim. Acta A 215 (2019) 348.

[3] S. Saha, S. Das, P. Sahoo, Chem. Select. 4 (2019) 13968.

[4] A. Sumiyoshi, Y. Chiba, R. Matsuoka, T. Noda, T. Nabeshima, Dalton Trans. 48 (2019) 13169-13175.

[5] L. Wang, Z.L. Wei, M. Yu, Y.Q. Pan, Y. Zhang, W.K. Dong, Chin. J. Inorg. Chem. 35 (2019) 1791.

[6] X.X. An, C. Liu, Z.Z. Chen, K.F. Xie, W.K. Dong, Crystals 9 (2019) 602.

[7] G. Kumar, D. Kumar, S. Devi, R. Johari, C.P. Singh, Eur. J. Med. Chem. 45 (2010) 3056.

[8] M.J. Timm, L. Leung, K. Anggara, T. Lim, Z. Hu, S. Latini, A. Rubio, J.C. Polanyi, J. Am. Chem. Soc. 142 (2020) 9453.

[9] V. Raju, R.S. Kumar, Y. Tharakeswar, S.K.A. Kumar, Inorg. Chim. Acta 493 (2019) 49.

[10] S. Mondal, S.M. Mandal, D. Ojha, D. Chattopadhyay, C. Sinha, Polyhedron 172 (2019) 28.

[11] H.R. Mu, M. Yu, L. Wang, Y. Zhang , Y.J. Ding, Phosphorus Sulfur Silicon Relat. Elem. 195 (2020) 730.

[12] Y.X. Sun, Y.Q. Pan, X. Xu, Y. Zhang, Crystals 9 (2019) 607.

[13] S.Z. Zhang, J. Chang, H.J. Zhang, Y.X. Sun, Y. Wu, Y.B. Wang, Chin. J. Inorg. Chem. 36 (2020) 503.

[14] Q.P. Kang, X.Y. Li, L. Wang, Y. Zhang, W.K. Dong, Appl. Organomet. Chem. 33 (2019) e5013.

[15] Y.Q. Pan, X. Xu, Y. Zhang, Y. Zhang, W.K. Dong, Spectrochim. Acta A 229 (2020) 117927.

[16] Y.F. Cui, Y. Zhang, K.F. Xie, W.K. Dong, Crystals 9 (2019) 596.

[17] P.K. Muwal, A. Nayal, M.K. Jaiswal, P.S. Pandey, Tetrahedron Lett. 59 (2018) 29.

[18] S. Maity, M. Shyamal, R. Maity, N. Mudi, P. Hazra, P.K. Giri, S.S. Samanta, S. Pyne, A. Misra, Photochem. Photobiol. Sci. 19 (2020) 681.

[19] V. Kumar, S. Kundu, B. Sk, A. Patra, New J. Chem. 43 (2019) 18582.

[20] S. Khanra, S. Ta, M. Ghosh, S. Chatterjee, D. Das, RSC Adv. 9 (2019) 21302.

[21] B. Das, A. Jana, A. Das Mahapatra, D. Chattopadhyay, A. Dhara, S. Mabhai, S. Dey,

Spectrochim. Acta A 212 (2019) 222.

[22] J.B. Chae, H. Lee, C. Kim, J. Fluores. 30 (2020) 347.

[23] K. Aich, S. Das, S. Gharami, L. Patra, T.K. Mondal, Chem.Select 4 (2019) 8068.

[24] T.W. Chen, U. Rajaji, S.M. Chen, J.Y. Wang, Z.A. Alothman, M.A. Ali, S.M. Wabaidur, F.A. Hemaid, S.Y. Lee, W.H. Chang, Ultrason. Sonochem. 66 (2020) 1350.

[25] G.J. Park, H. Kim, J.J. Lee, Y.S. Kim, S.Y. Lee, S. Lee, I. Noh, C. Kim, Sens. Actuators B 215 (2015) 568.

[26] H.R. Mu, X.X. An, C. Liu, Y. Zhang, W.K. Dong, J. Struct. Chem. 61 (2020) 1155.

[27] A. Kumar, S. Kumar, P.S. Chae, Dyes Pigm. 181 (2020) 108522.

[28] Y. Zhang, Y.Q. Pan, M. Yu, X. Xu, W.K. Dong, Appl. Organomet. Chem. 33 (2019) e5240.

[29] Z.Y. Gündüz, C. Gündüz, C. Özpınar, O.A. Urucu, Spectrochim. Acta A 136 (2015) 1679.

[30] Y. Zhang, L.Z. Liu, Y.D. Peng, N. Li, W.K. Dong, Transit. Met. Chem. 44 (2019) 627.

[31] S. Akine, Z. Varadi, T. Nabeshima, Eur. J. Inorg. Chem. 2013 (2013) 5987.

[32] T. Nakamura, S. Tsukuda, T. Nabeshima, J. Am. Chem. Soc. 141 (2019) 6462.

[33] Y. Zhang, M. Yu, Y.Q. Pan, Y. Zhang, L. Xu, X.Y. Dong, Appl. Organomet. Chem. 34 (2020) e5442.

[34] L. Wang, Z.L. Wei, C. Liu, W.K. Dong, J.X. Ru, Spectrochim. Acta A 239 (2020) 118496.

[35] M. Yu, Y. Zhang, Y.Q. Pan, L. Wang, Inorg. Chim. Acta 509 (2020) 119701.

[36] C.J. Chandler, L.W. Deady, J.A. Reiss, J. Heterocyclic Chem. 18 (1981) 599.

[37] S. Tursunbadalov, L. Soliev, J. Chem. Eng. Data 63 (2018) 598.

[38] H. Morito, S. Shibano, T. Yamada, T. Ikeda, M. Terauchi, R.V. Belosludov, H. Yamane, Solid State Sci. 102 (2020) 106166.

[39] C.A. Huerta-Aguilar, T. Pandiyan, N. Singh, N. Jayanthi, Spectrochim. Acta A 146 (2015) 142.

[40] T.S. Ortner, K. Wurst, M. Seibald, B. Joachim, H. Huppertz, Eur. J. Inorg. Chem. 2016 (2016) 3292.

[41] X.X. An, Z.Z. Chen, H.R. Mu, L. Zhao, Inorg. Chim. Acta 511 (2020) 119823.

[42] R.N. Bian, J.F. Wang, Y.J. Li, Y. Zhang, W.K. Dong, J. Photochem. Photobiol. A. 400 (2020) 112829.

[43] X. Xu, R.N. Bian, S.Z. Guo, W.K. Dong, Y.J. Ding, Inorg. Chim. Acta 513 (2020) 119945.

[44] L. Wang, Y.Q. Pan, J.F. Wang, Y. Zhang, Y.J. Ding, J. Photochem. Photobio. A 400 (2020) 112719.

[45] L. Wang, Z.L. Wei, Z.Z. Chen, C. Liu, W.K. Dong, Y.J. Ding, Microchem. J. 155 (2020) 104801.

[46] Z.L. Wei, L. Wang, J.F. Wang, W.T. Guo, Y. Zhang, W.K. Dong, Spectrochim. Acta A 228 (2020) 117775.

[47] R.T. loto, C.A. Loto, M. Akinyele, Alex. Eng. J. 59 (2020) 933.

[48] Z.L. Wei, L. Wang, S.Z. Guo, Y. Zhang, W.K. Dong, RSC Adv. 9 (2019) 41298.

[49] F.S. Carlos, L.A. Silva, C. Zanlorenzi, F.S. Nunes, Inorg. Chim. Acta 508 (2020) 119634.

[50] H.A. Saudi, W.M. Abd-Allah, K.S. Shaaban, J. Mater. Sci. Mater. Electron 31 (2020) 6963.

[51] M. Yu, H.R. Mu, L.Z. Liu, N. Li, Y. Bai, X.Y. Dong, Chin. J. Inorg. Chem. 35 (2019) 1109.

[52] F. Risplendi, F. Raffone, L.C. Lin, J.C. Grossman, G. Cicero, J. Phys. Chem. C 124 (2020) 1438.

[53] L. Xu, M. Yu, L.H. Li, J.C. Ma, W.K. Dong, J. Struct. Chem. 60 (2019) 1358.

[54] K.G. Yves, T. Chen, J.T. Aladejana, Z. Wu, Y. Xie, ACS Omega 5 (2020) 8784.

[55] J. Chang, S.Z. Zhang, Y. Wu, H.J. Zhang, Y.X. Sun, Transit. Met. Chem. 45 (2020) 279.

[56] A. Vera, J.L. Moreno, C. Garcia, D. Morais, F. Bastida, Sci. Total Environ. 685 (2019) 564.

[57] M. Tian, H. He, B.B. Wang, X. Wang, Y. Liu, F.L. Jiang, Dyes Pigm. 165 (2019) 383.

[58] M. Sahu, A.K. Manna, K. Rout, J. Modal, G.K. Patra, Inorg. Chim. Acta 508 (2020) 119633.

[59] H.A. Carlos Alberto, R.G. Brayan, T. Pandiyan, N. Jayanthi, S. Narinder, Photochem. Photobiol. Sci. 18 (2019) 1761.

[60] Y.Q. Pan, Y. Zhang, M. Yu, Y. Zhang, L. Wang, Appl. Organomet. Chem. 34 (2020) e5441.

[61] L.W. Zhang, Y. Zhang, Y.F. Cui, M. Yu, W.K. Dong, Inorg. Chim. Acta 506 (2020) 119534.

[62] A.K. Manna, K. Rout, S. Chowdhury, G.K. Patra, Photochem. Photobio. Sci. 18 (2019) 1512.

[63] C. Liu, X.X. An, Y.F. Cui, K.F. Xie, W.K. Dong, Appl. Organomet. Chem. 34 (2019) e5272.

[64] F. Spadaro, A. Rossi, S.N. Ramakrishna, E. Laine, P. Woodward, N.D. Spencer, Langmuir. 34 (2018) 2219.

[65] L.Z. Liu, M. Yu, X.Y. Li, Q.P. Kang, W.K. Dong, Chin. J. Inorg. Chem. 35 (2019) 1283.

[66] S.S Kumar, R.S. Kumar, S.K.A. Kumar, Inorg. Chim. Acta 502 (2020) 119348.

[67] W. Du, C.M. Jia, Y.F. Zhang, Q. Chen, Y.L. Wang, Y. Huang, Q. Zhang, Anal. Methods 10

(2020) 1993.

[68] C. Liu, Z.L. Wei, H.R. Mu, W.K. Dong, Y.J. Ding, J. Photochem. Photobio. A 397 (2020) 112569.

Table 1. Comparison of binding constants and detection lines between chemosensors.

No.	sensor	Binding constant (M^{-1})	Detection limit (M)	Identification substance	Reference
1	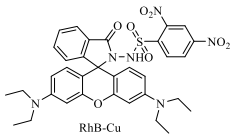	6.42×10^{4}	4.7×10^{-6}	Cu^{2+}	[57]
2	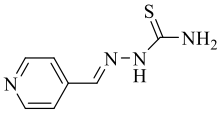	2.4×10^{2}	1.7×10^{-6}	Cu^{2+}	[58]
3	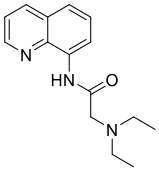	3.84×10^{7}	5.5×10^{-8}	$H_2PO_4^-$	[66]
4	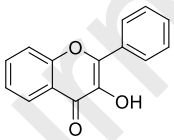	2.1×10^{5}	None	$H_2PO_4^-$	[67]
5	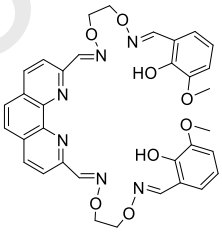	2.29×10^{13}	7.22×10^{-6}	Cu^{2+}	This work
		3.26×10^{9}	5.83×10^{-8}	$H_2PO_4^-$	This work

Conflicts of Interest: The authors declare no competing financial interests.

Research Highlights

1. An novel *O*-phenanthroline-based bis(half-salamo)-like fluorescent chemical sensor **L$_{POV}$** with two N_3O cavities was synthesized.

2. The sensor **Lpov** can detect quickly and efficiently Cu^{2+} and the **Lpov-Cu^{2+}** complex can continuously detect HPO_4^{2-} and $H_2PO_4^-$.

3. The order of the binding constant is as high as 10^{13} (Ka = 2.29×10^{13} M^{-1}).

No conflict of interest exits in the submission of this manuscript, and manuscript is approved by all authors for publication. I would like to declare on behalf of my co-authors that the work described was original research that has not been published previously, and not under consideration for publication elsewhere, in whole or in part. All the authors listed have approved the manuscript that is enclosed. In addition, we solemnly declare that the article is original and unpublished and is not being considered for publication elsewhere.

LEGENDS

Scheme 1 Synthesis route to **Lpov**

Fig. 1 Effect of the solvent system on the fluorescence intensity of the **Lpov**

Fig. 2 The effect of water content in solvent (DMF:H_2O, v/v) on the fluorescence intensity of **Lpov**

Fig. 3 Fluorescence spectra of **Lpov** and metal ions (20 equiv.) in DMF/H_2O buffer solution (**Lpov**, 1×10^{-3} mol/L; Tris-HCl buffer solution, 9/1, v/v, pH = 7.23)

Fig. 4 Fluorescence titration of Cu^{2+} in DMF/H_2O buffer solution with **Lpov**. (The inset shows a scatter plot of the fluorescence intensity of **Lpov** at 382 nm with Cu^{2+} concentration; **Lpov**, 1×10^{-3} mol/L; Tris-HCl buffer solution, 9/1, v/v, pH = 7.23).

Fig. 5 Benesi-Hildebrand fit curve of Cu^{2+} with **Lpov**

Fig. 6 Lpov (1×10^{-3} mol/L) in DMF/H_2O buffer solution for Cu^{2+} recognition anti-interference experiment. (Emission peak at 382 nm. The black bar is the fluorescence intensity of **Lpov** at 382 nm after adding common metal ion, the red bar is the fluorescence intensity of the **Lpov-3Cu^{2+}** complex after adding common metal ion. **Lpov**, 1×10^{-3} mol/L; cation, 1×10^{-2} mol/L; Tris-HCl buffer solution, 9/1, v/v, pH = 7.23).

Fig. 7 The pH response of **Lpov** and Cu^{2+} in fluorescent chemical sensors (**Lpov**, 1×10^{-3} mol/L; Tris-HCl buffer solution, 9/1, v/v)

Fig. 8 Time response diagram of interaction between **Lpov** and Cu^{2+} in fluorescent chemical sensor (**Lpov**, 1×10^{-3} mol/L; Tris-HCl buffer solution, 9/1, v/v, pH = 7.23).

Fig. 9 Job working curve of Cu^{2+} on **Lpov** (**Lpov**, 1×10^{-3} mol/L; Tris-HCl buffer solution, 9/1, v/v, pH = 7.23)

Fig. 10 ESI-MS spectrum (a) ESI-MS spectrum of **Lpov**; (b) ESI-MS spectrum of the **Lpov-3Cu^{2+}** complex

Fig. 11 Proposed recognition mechanism of Cu^{2+} by **Lpov**

Fig. 12 Molecular orbital energy diagrams of **L$_{POV}$** and the **Lpov-3Cu^{2+}** complex. (a) Molecular orbital energy diagram of **L$_{POV}$**. (b) Molecular orbital energy diagram of the **Lpov-3Cu^{2+}** complex

Fig. 13 Determination of Cu^{2+} in tap water sample (n = 3; **Lpov**, 1×10^{-3} mol/L).

Fig. 14 The **Lpov-3Cu^{2+}** complex (1×10^{-3} mol/L) in DMF/H_2O buffer solution for HPO_4^{2-}/$H_2PO_4^-$ recognition anti-interference experiment. (Emission peak at 382 nm. The black bar is the fluorescence intensity of **L$_{POV}$**, the red bar is the fluorescence intensity of **L$_{POV}$** with Cu^{2+} added, the blue bar is the fluorescence intensity of the **Lpov-3Cu^{2+}** complex after adding common metal anions, the pink bar is the fluorescence intensity of **L$_{POV}$** after adding common metal anions. **L$_{POV}$**, 1×10^{-3} mol/L; cation, 1×10^{-2} mol/L; Tris-HCl buffer solution, 9/1, v/v, pH = 7.23).

Fig. 15 Molecular orbital energy diagrams of the **2Lpov-Cu^{2+}** complex.

Fig. 16 Fluorescence titration of $H_2PO_4^-$ in DMF/H_2O buffer solution with the **Lpov-3Cu^{2+}** complex. (The **Lpov-3Cu^{2+}** complex, 1×10^{-3} mol/L; cation, 1×10^{-2} mol/L; Tris-HCl buffer solution, 9/1, v/v, pH = 7.23).

Fig. 17 Job working curve of $H_2PO_4^-$ on the **Lpov-3Cu^{2+}** complex

Fig. 18 ESI-MS spectrum (a) ESI-MS spectrum of the **2Lpov-Cu^{2+}** complex (HPO_4^{2-}); (b) ESI-MS spectrum of the **2Lpov-Cu^{2+}** complex ($H_2PO_4^-$)

Fig. 19 Proposed recognition mechanism of HPO_4^{2-}/$H_2PO_4^-$ by the **Lpov-3Cu^{2+}** complex

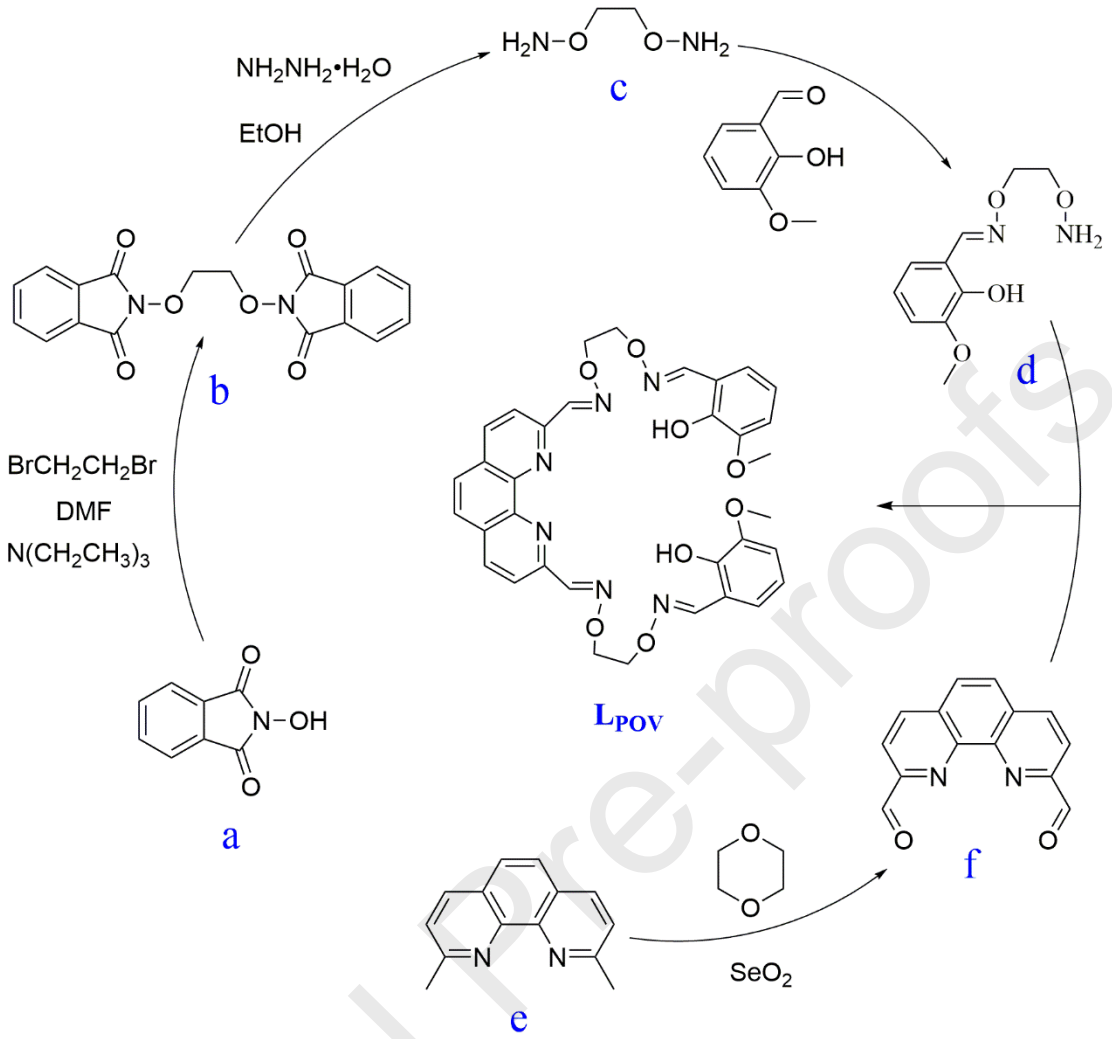
NH2NH2•H2O
EtOH
H2N–O O–NH2
c
OH
O
d
NH2
b
BrCH2CH2Br
DMF
N(CH2CH3)3
HO
LPOV
N–OH
a
f
SeO2
e

Scheme 1

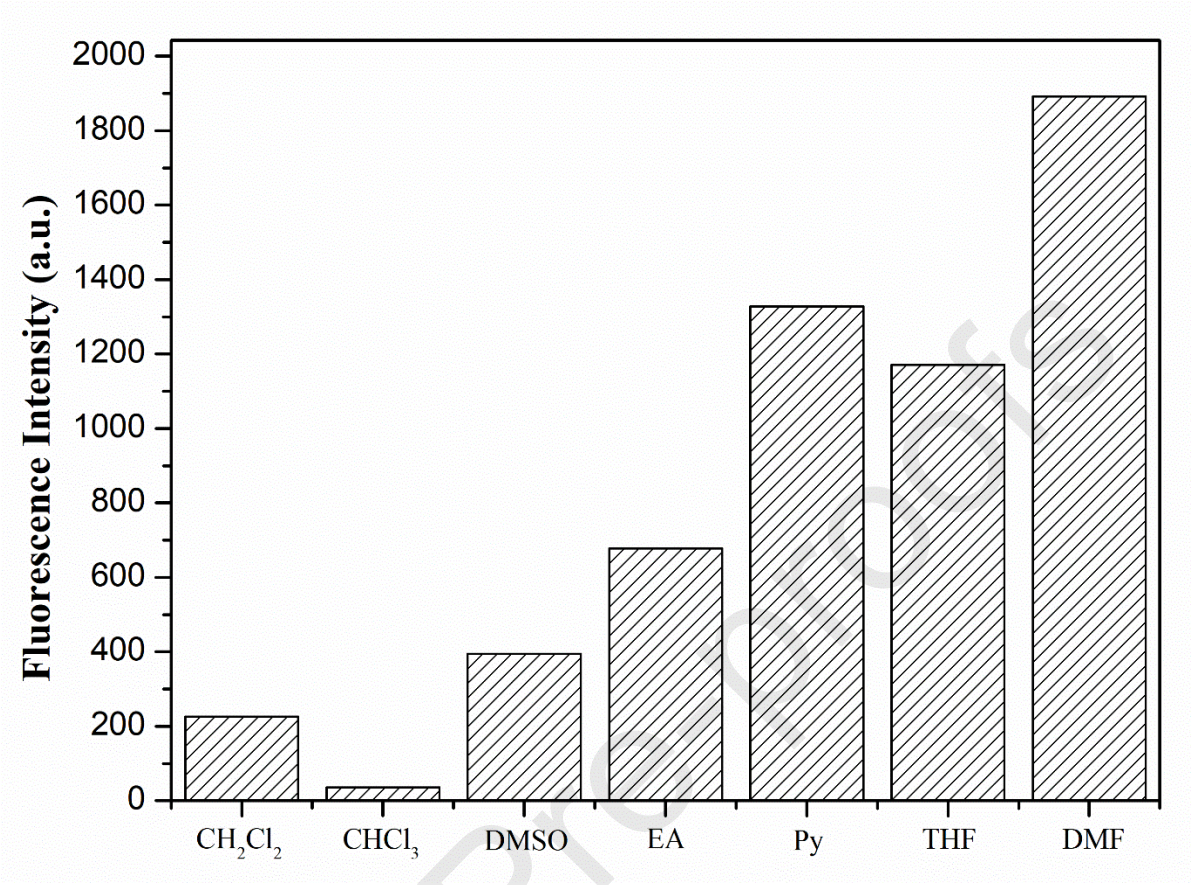

Fig. 1

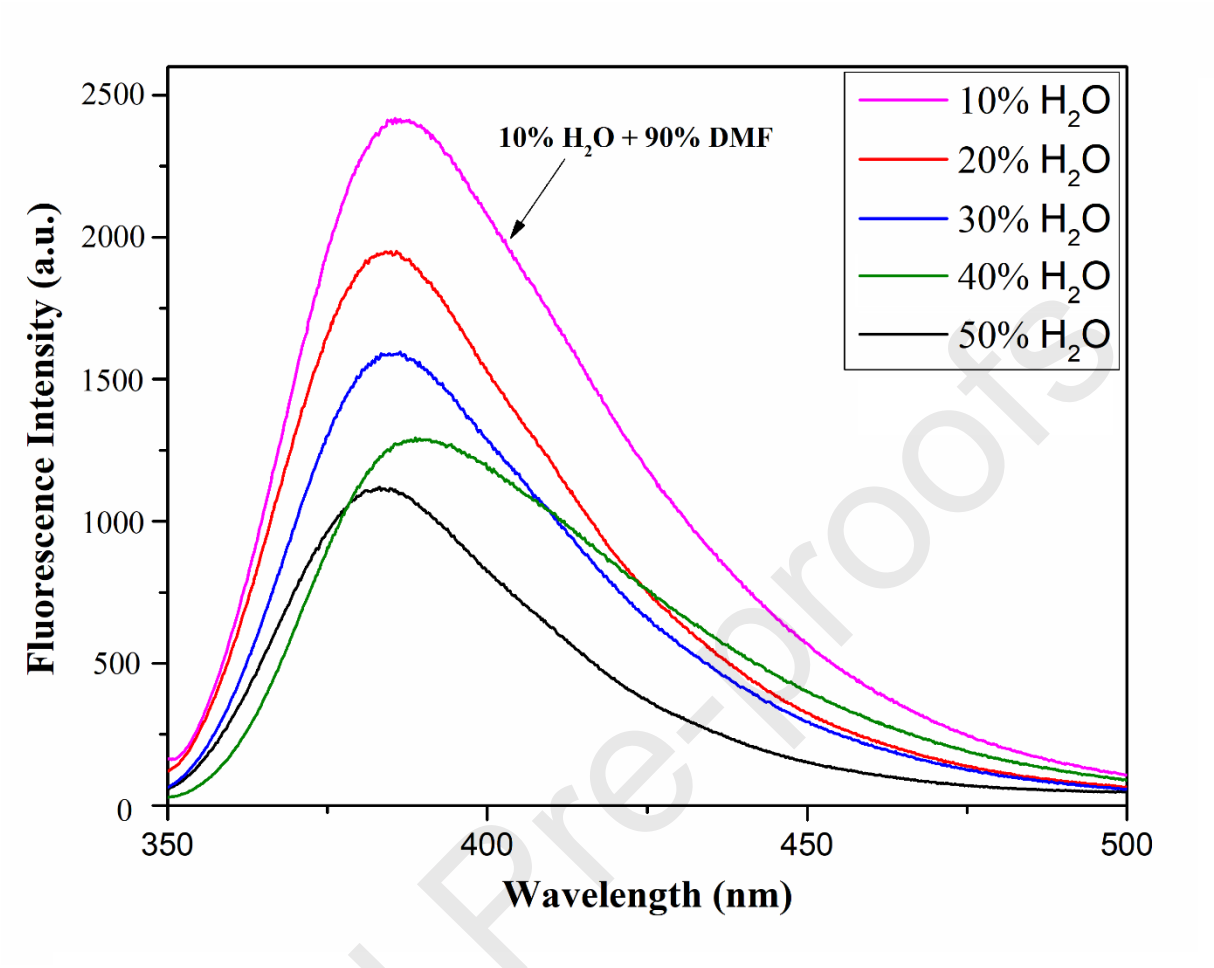

Fig. 2

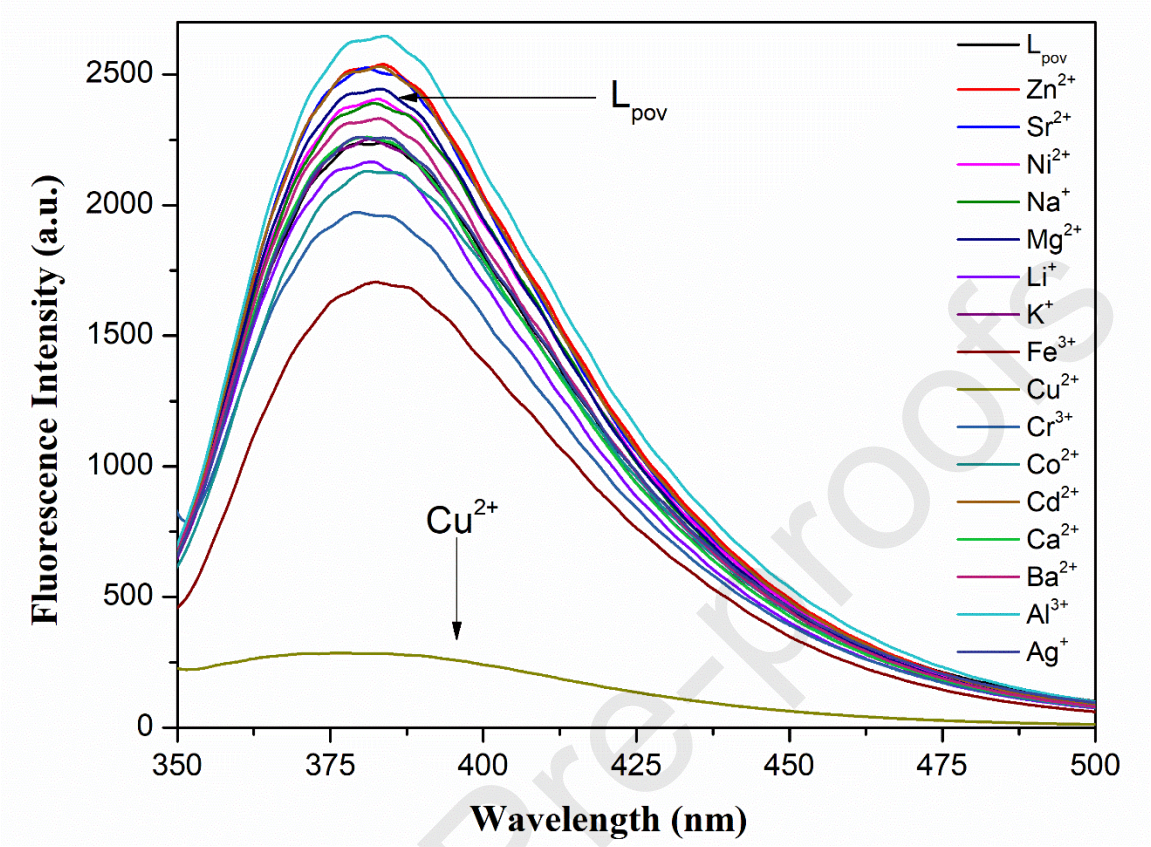

Fig. 3

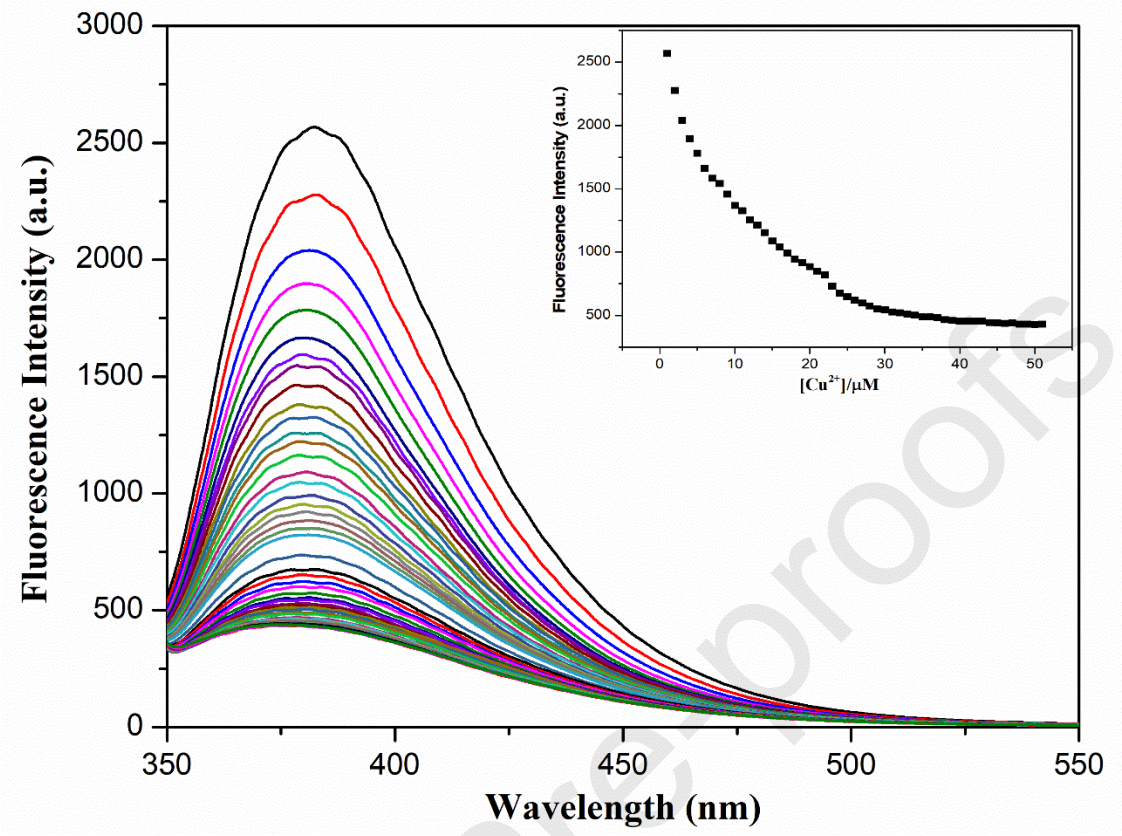

Fig. 4

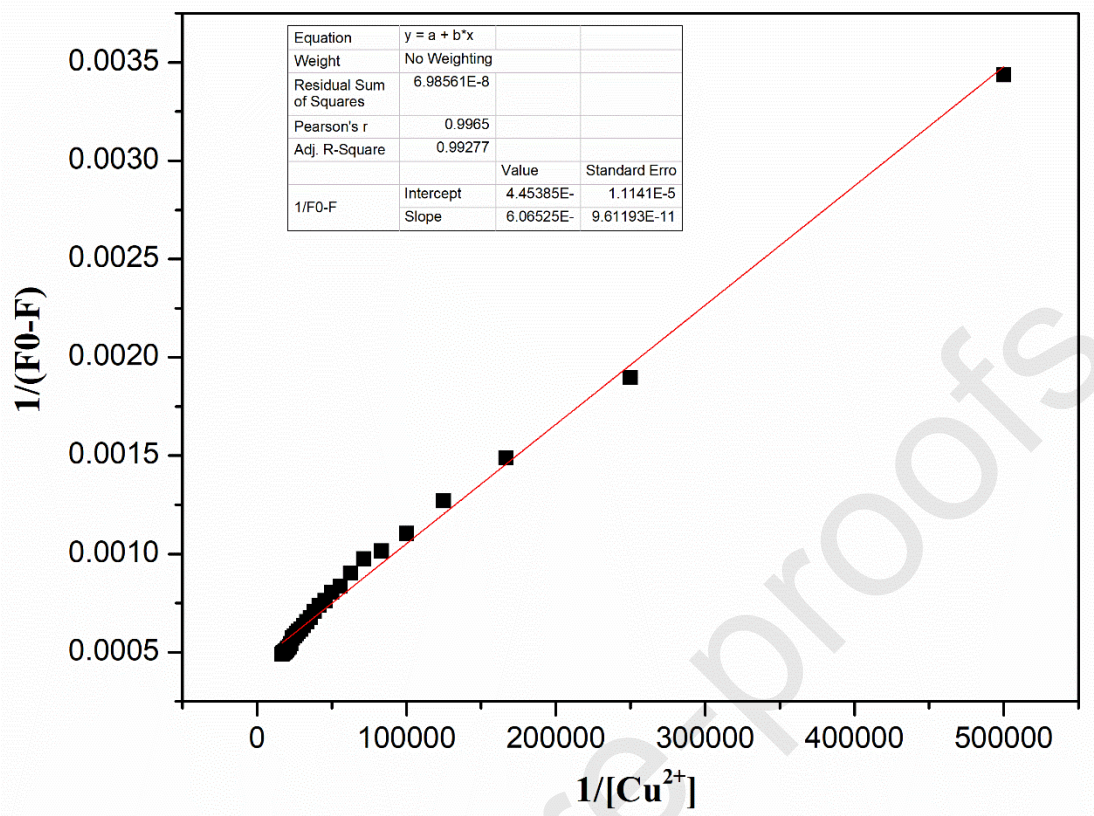

Fig. 5

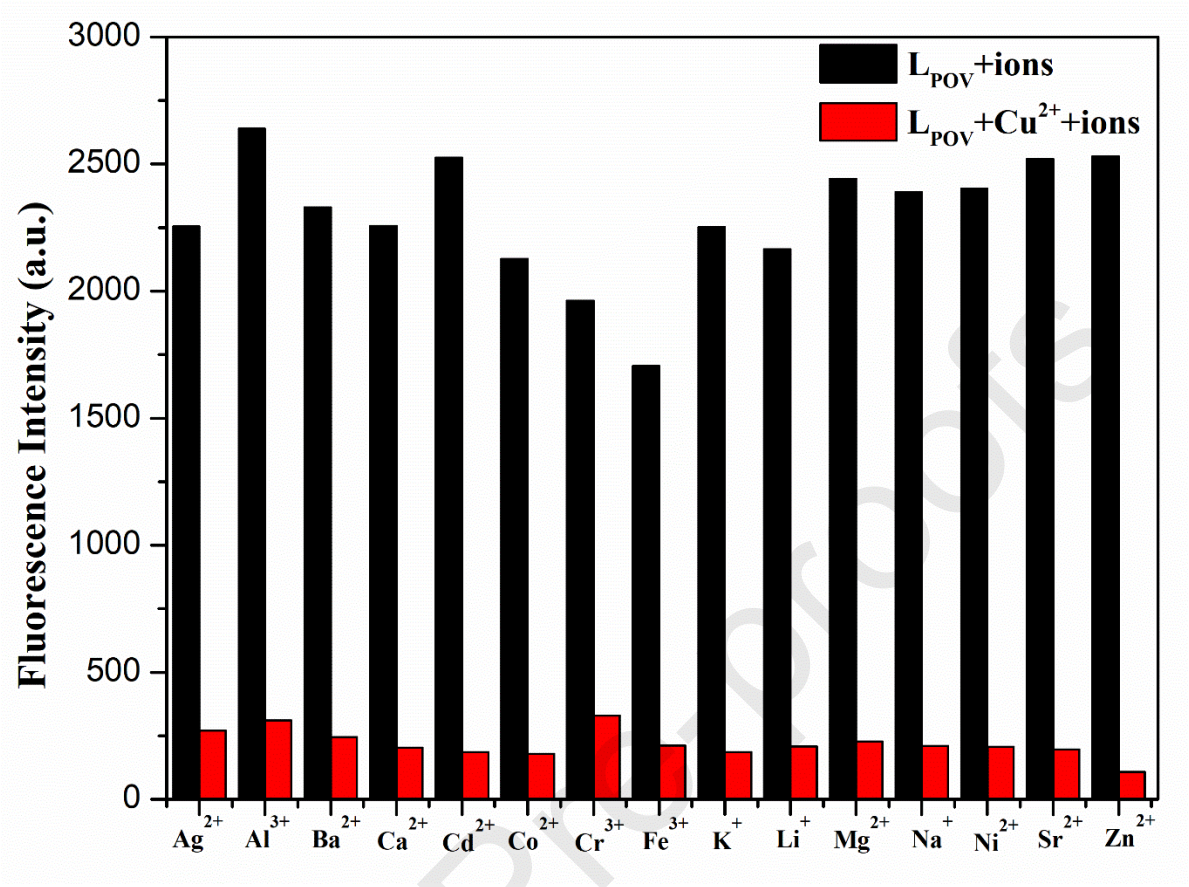

Fig. 6

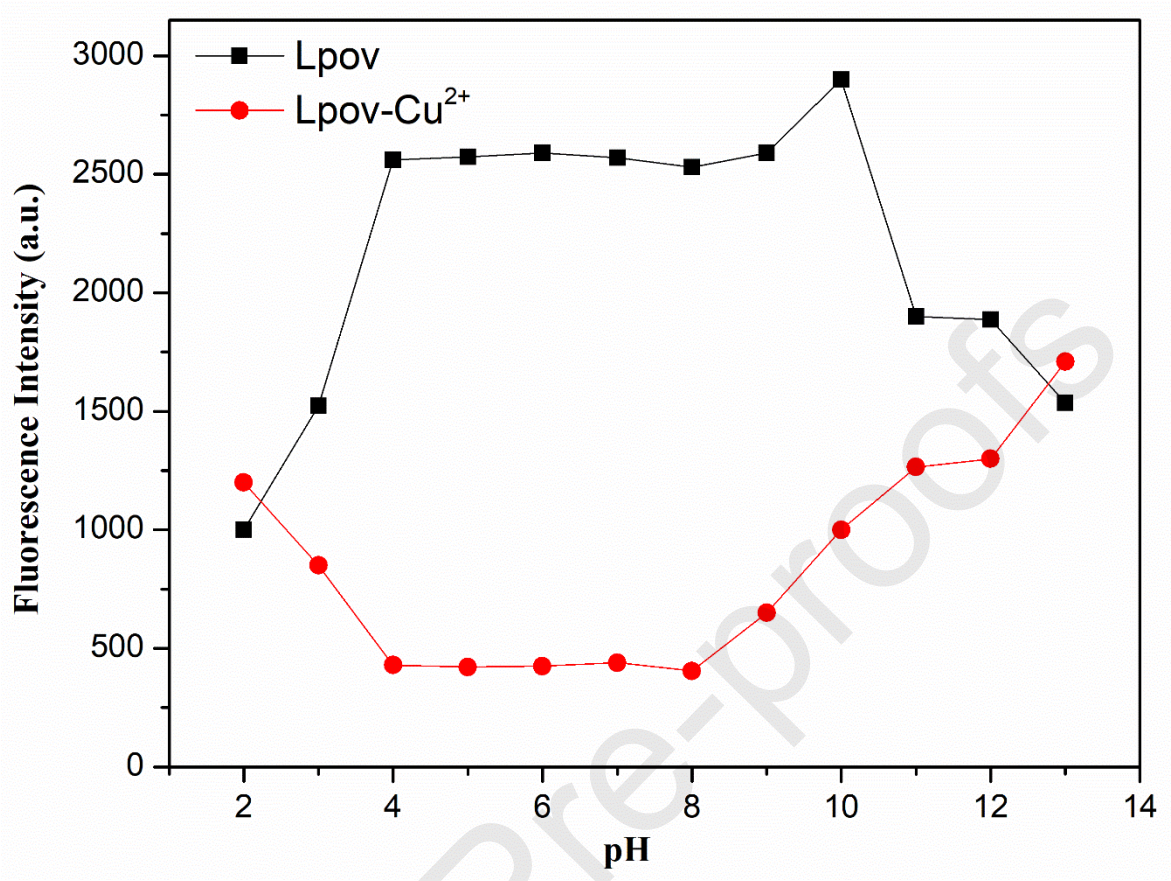

Fig. 7

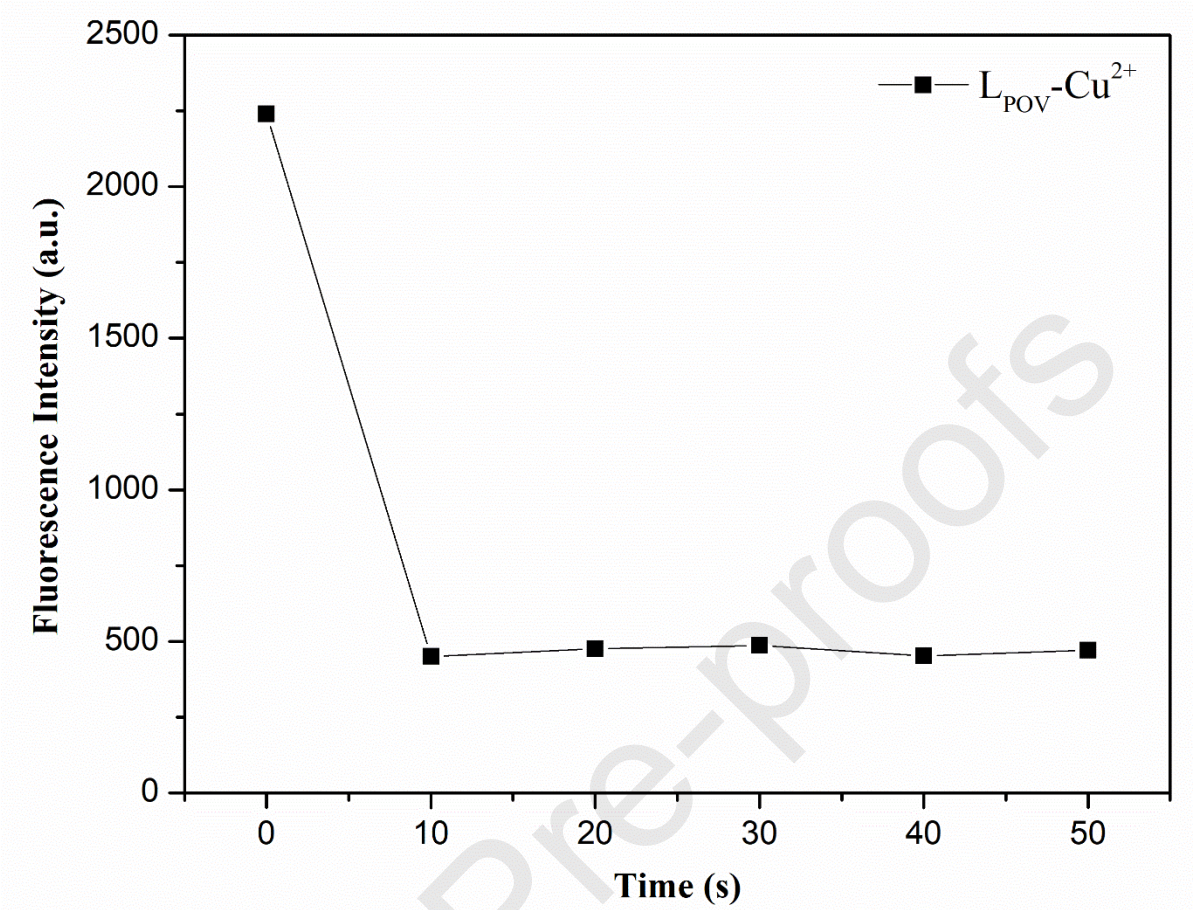

Fig. 8

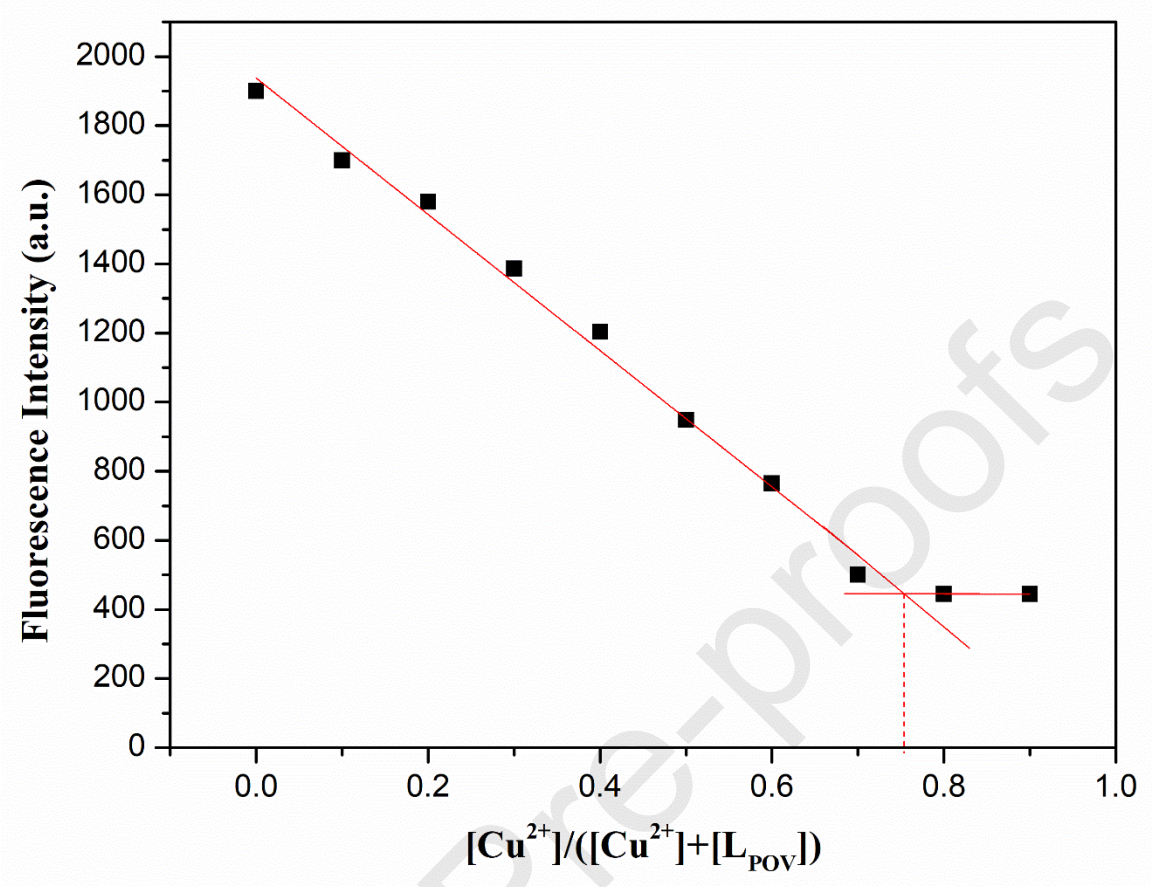

Fig. 9

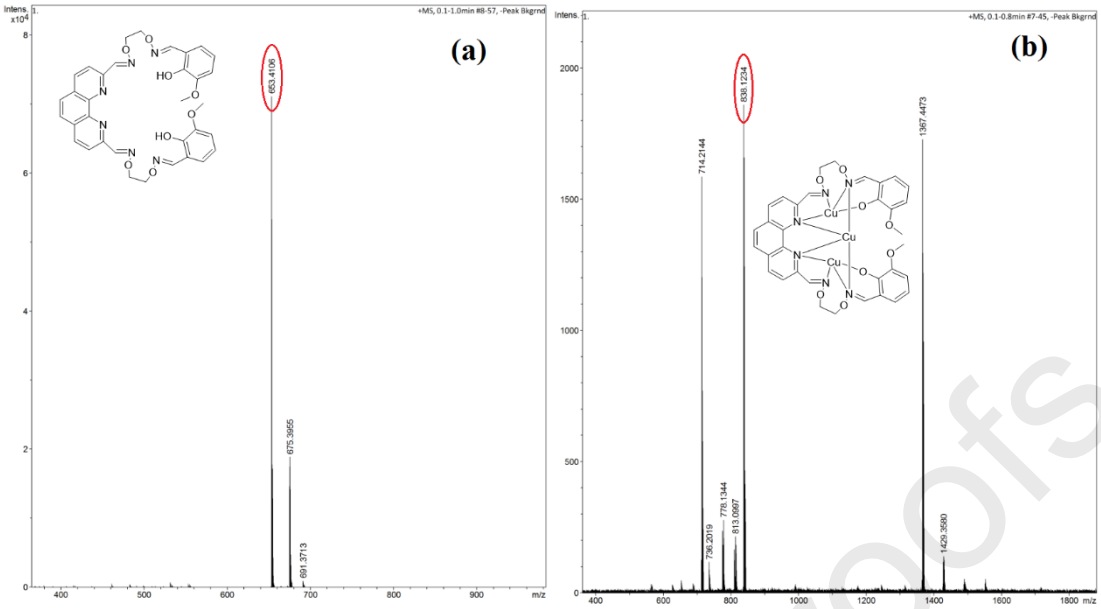

Fig. 10

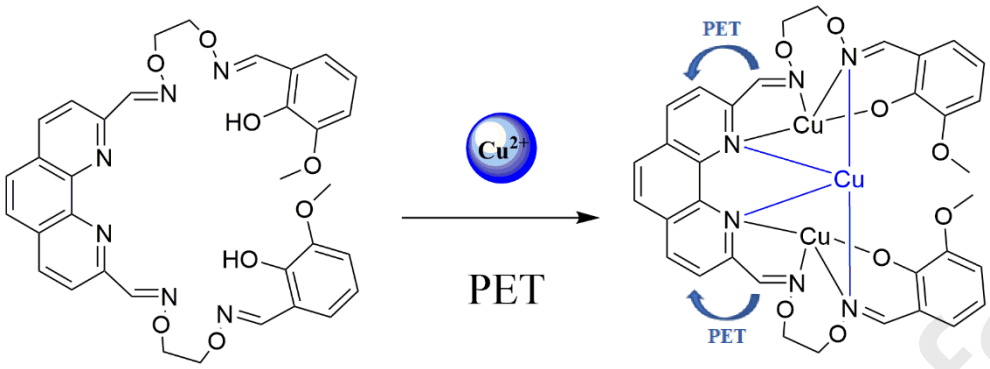

Fig. 11

Molecular orbital		
Energy (eV)		Energy (eV)
-1.26504	LUMO+2	
-1.76028	LUMO+1	
0.40299	ΔE	
-2.16327	LUMO	
3.69471	ΔE	
-5.85798	HOMO	
0.05170	ΔE	
-5.90968	HOMO-1	
-5.95594	HOMO-2	

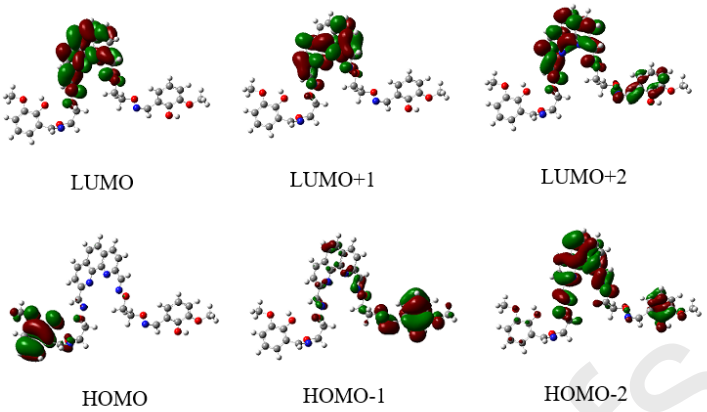

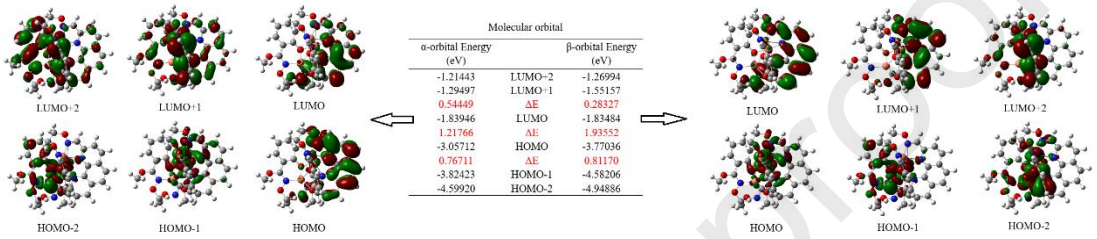

Molecular orbital		
α-orbital Energy (eV)		β-orbital Energy (eV)
-1.21443	LUMO+2	-1.26994
-1.29497	LUMO+1	-1.55157
0.54449	ΔE	0.28327
-1.83946	LUMO	-1.83484
1.21766	ΔE	1.93552
-3.05712	HOMO	-3.77036
0.76711	ΔE	0.81170
-3.82423	HOMO-1	-4.58206
-4.59920	HOMO-2	-4.94886

Fig. 12

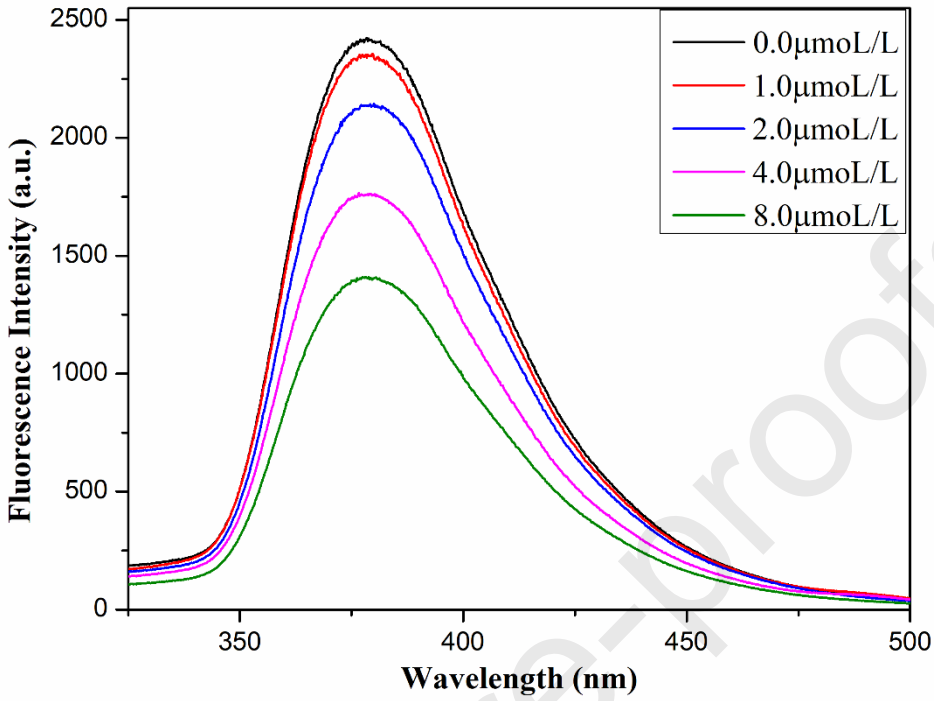

Added Cu^{2+} ($\mu mol \cdot L^{-1}$)	Found ($\mu mol \cdot L^{-1}$)	Recovery(%)	R.S.D.(n=3) (%)
0	Not detected		
1.0	0.927	92.70	3.5
2.0	1.933	96.65	1.3
4.0	3.961	99.03	1.8
8.0	7.875	98.44	2.7

Fig. 13

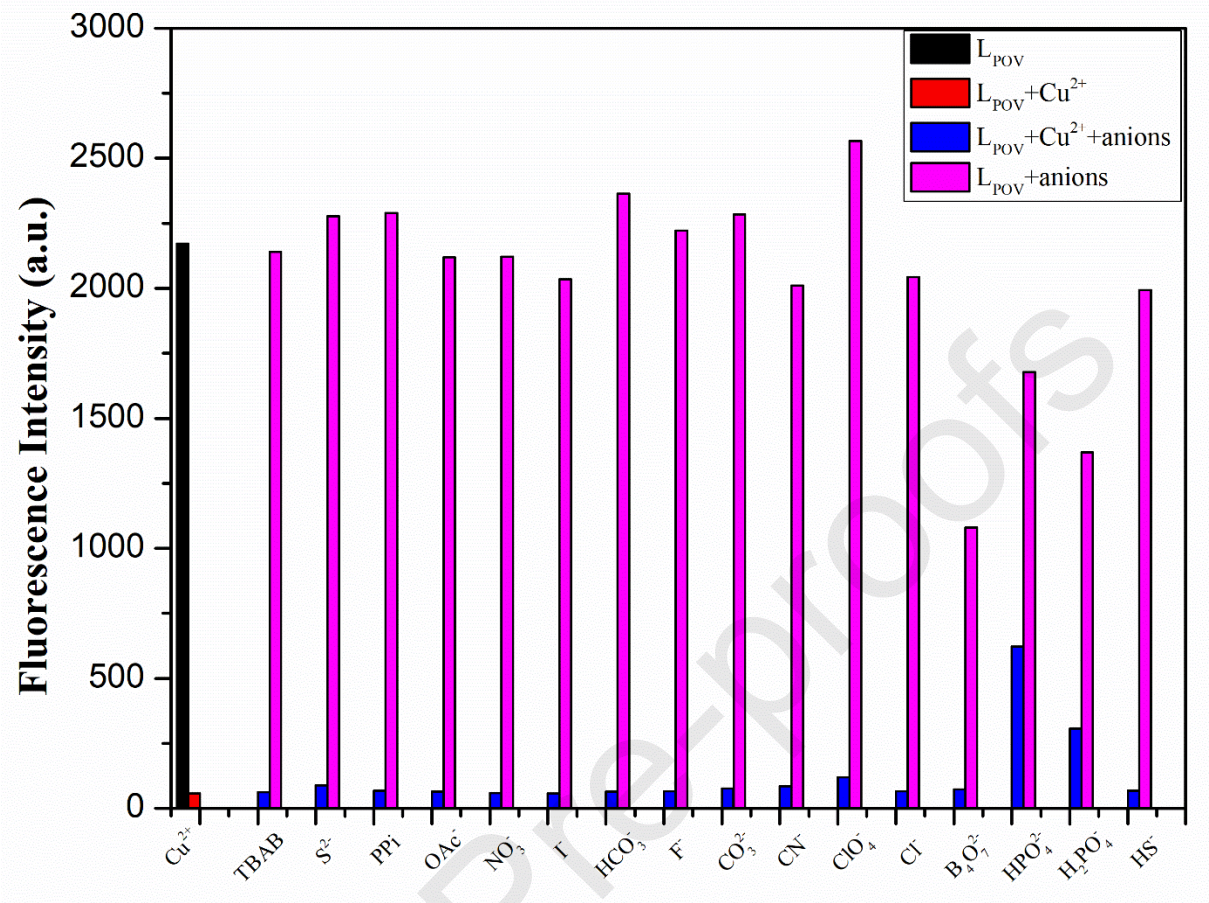

Fig. 14

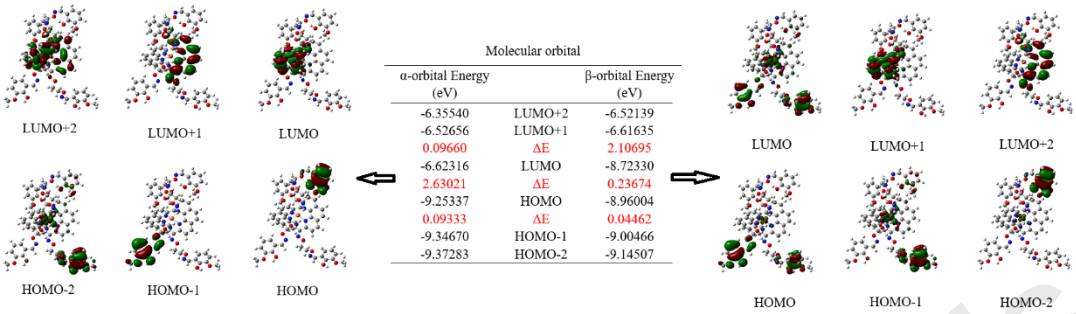

Molecular orbital		
α-orbital Energy (eV)		β-orbital Energy (eV)
-6.35540	LUMO+2	-6.52139
-6.52656	LUMO+1	-6.61635
0.09660	ΔE	2.10695
-6.62316	LUMO	-8.72330
2.63021	ΔE	0.23674
-9.25337	HOMO	-8.96004
0.09333	ΔE	0.04462
-9.34670	HOMO-1	-9.00466
-9.37283	HOMO-2	-9.14507

Fig. 15

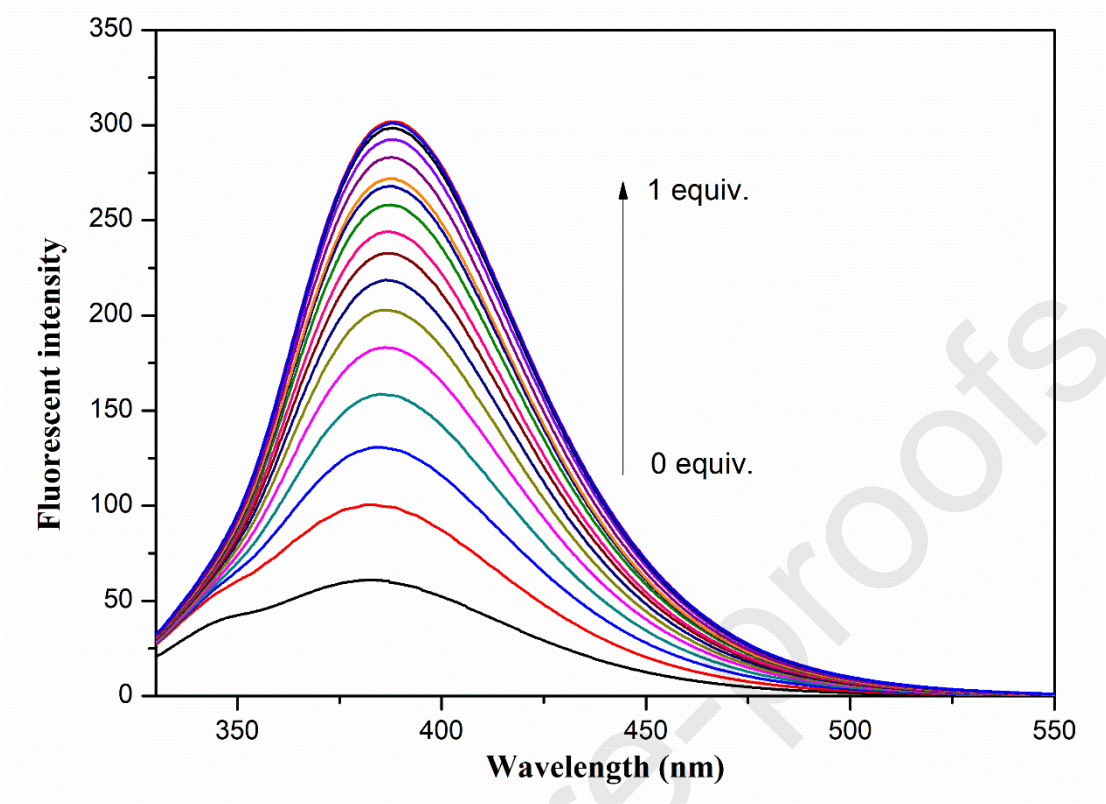

Fig. 16

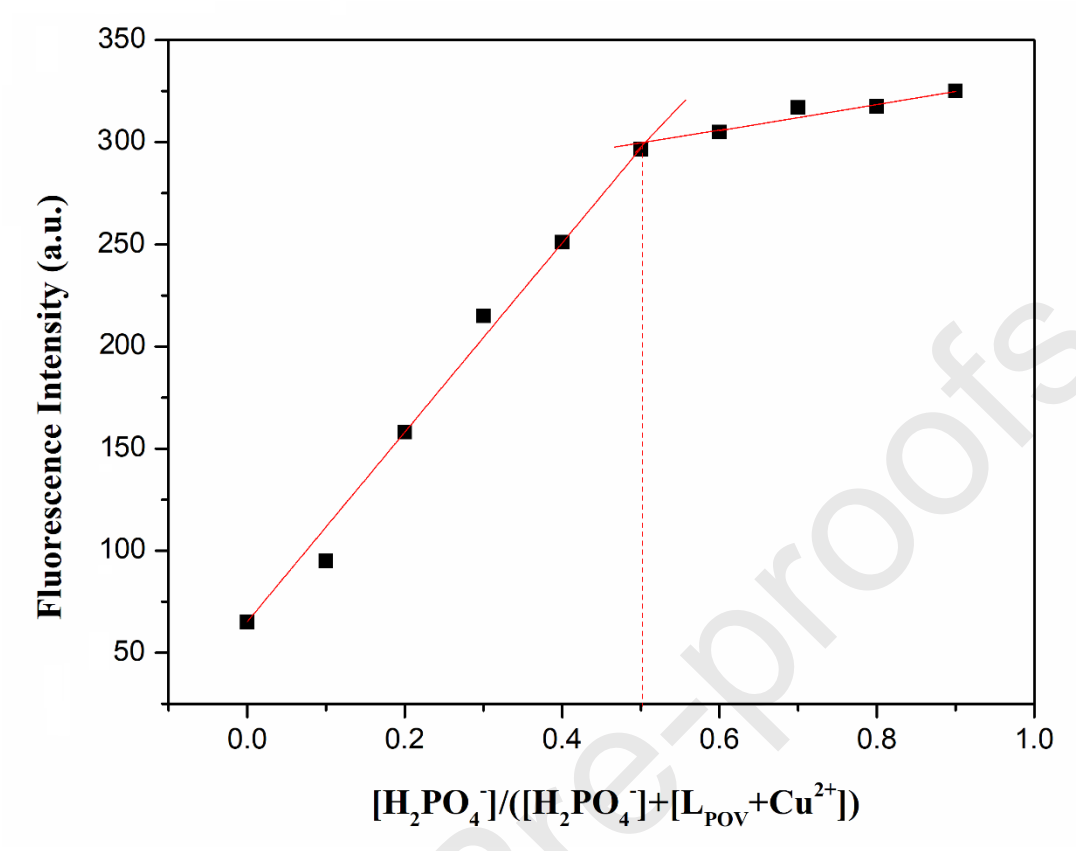

Fig. 17

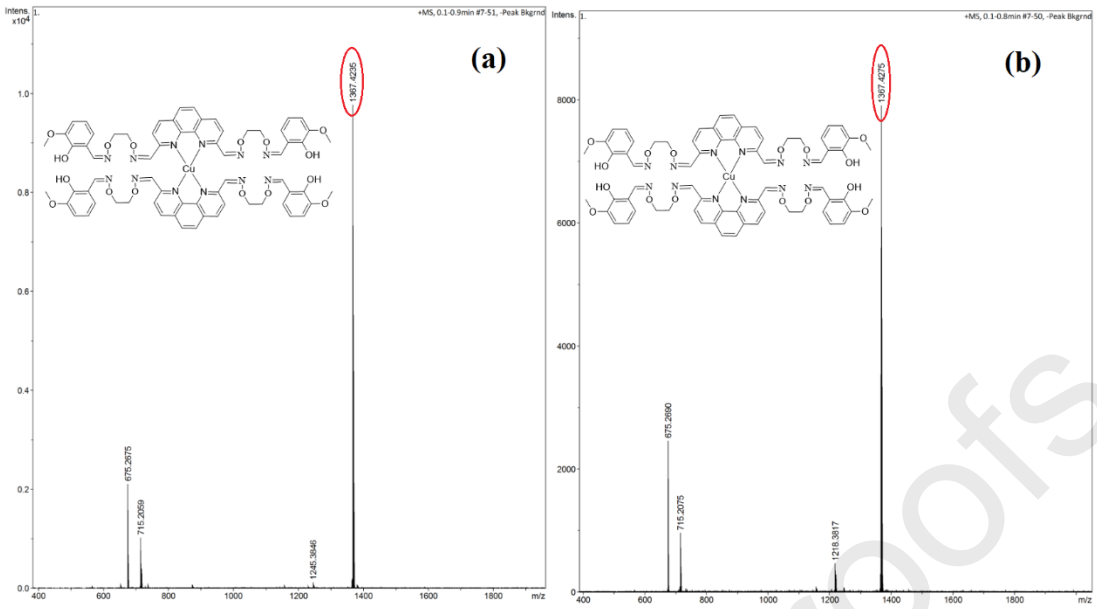

Fig. 18

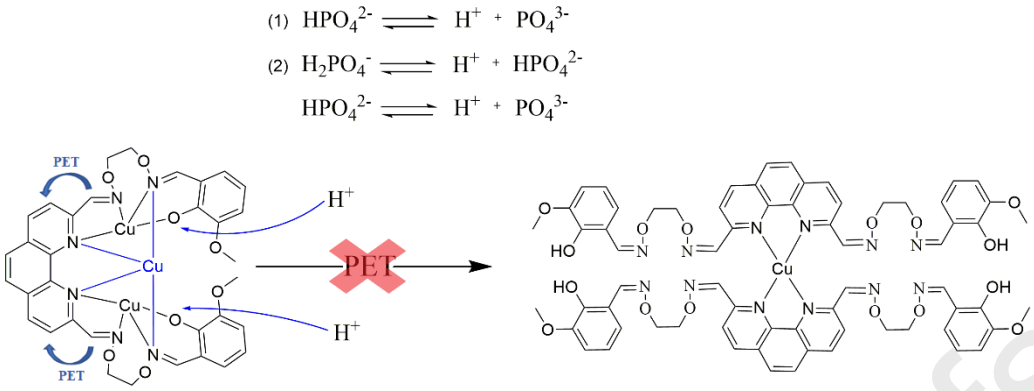

Fig. 19

Graphical Abstract

An *O*-phenanthroline-based bis(half-salamo)-like fluorescent chemical sensor **L_{POV}** with two N_3O cavities was synthesized. The chemical sensor **Lpov** can detect Cu^{2+} by the phenomenon of fluorescence quenching and the **Lpov-3Cu^{2+}** complex can continuously detect HPO_4^{2-} and $H_2PO_4^-$. Different from the traditional N_2O_2 cavity of salamo-like compound, the introduction of *O*-phenanthroline N atoms with stronger coordination ability makes the coordination mode of the sensor molecule more novel and provides more possibilities for the coordination modes.

Probe for the detection of $Cu^{2+}$and HPO_4^{2-}/$H_2PO_4^-$:

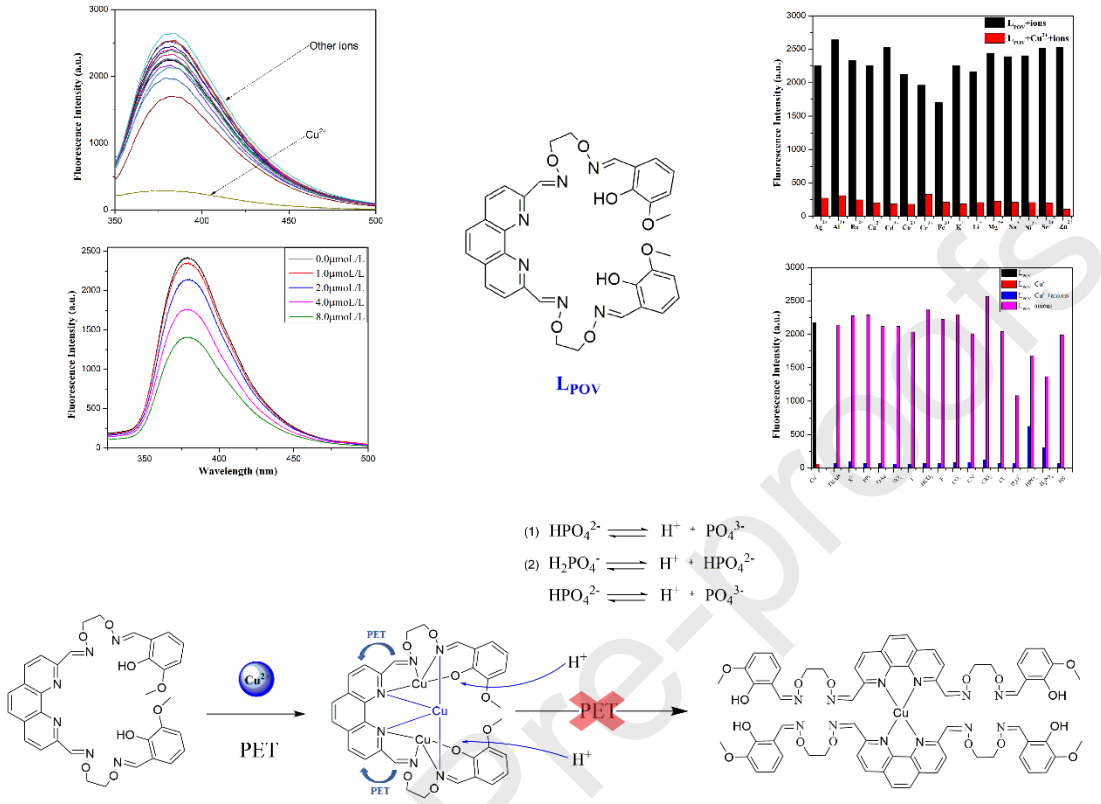

Biographies

Ruo-Nan Bian is currently pursuing her master's degree in the School of Chemical and Biological Engineering at Lanzhou Jiaotong University, China. She obtained her B.S.in the School of Chemical and Biological Engineering at Lanzhou Jiaotong University, China, in 2017.

Xin Xu is currently pursuing her master's degree in the School of Chemical and Biological Engineering at Lanzhou Jiaotong University, China. She obtained her bachelor's degree in the School of Chemistry and Chemical Engineering of Jining University, China, in 2018.

Tao Feng is currently pursuing his master's degree in the School of Chemical and Bio logical Engineering at Lanzhou Jiaotong University, China. He obtained his B.S.in the College of Chemical Engineering, Shanxi Datong University, China in 2017.

Wen-Kui Dong received his PhD degree in 1998 from Lanzhou University, China. He is a professor in the School of Chemical and Biological Engineering at Lanzhou Jiaotong University. His current research interests are focusing on the chemistry of functional supramolecular complexes, materials and new products, as well as

processes and applications of environmental chemical engineering.